Importance of air cavity ventilation on pressures and forces on vertical structure subject to overflow

Kim, Taeksang; Malherbe, Julien; Plescher, Ries; Shimpalee, Sirawit; Felder, Stefan; Bricker, Jeremy

DOI
10.1080/21664250.2024.2407700

Publication date
2024

Document Version
Final published version

Published in
Coastal Engineering Journal

Citation (APA)
Kim, T., Malherbe, J., Plescher, R., Shimpalee, S., Felder, S., & Bricker, J. (2024). Importance of air cavity ventilation on pressures and forces on vertical structure subject to overflow. *Coastal Engineering Journal*, *66*(4), 703-724. Article 2407700. https://doi.org/10.1080/21664250.2024.2407700

COASTAL ENGINEERING JOURNAL
https://doi.org/10.1080/21664250.2024.2407700

Importance of air cavity ventilation on pressures and forces on vertical structure subject to overflow

Taeksang Kim[a], Julien Malherbe[a], Ries Plescher[a], Sirawit Shimpalee[b], Stefan Felder[c] and Jeremy Bricker[a,d]

[a]Department of Civil and Environmental Engineering, University of Michigan, Ann Arbor, MI, USA; [b]Department of Naval Architecture and Marine Engineering, University of Michigan, Ann Arbor, MI, USA; [c]Water Research Laboratory, School of Civil and Environmental Engineering, UNSW Sydney, Manly Vale, Australia; [d]Department of Hydraulic Engineering, Faculty of Civil Engineering & Geosciences, Delft University of Technology, Delft, The Netherlands

ABSTRACT

This study investigates the dynamics of air-water flow and the resulting forces on a broad-crested weir with a vertical face under both ventilated and non-ventilated cavity conditions. The focus is on measured forces and flow characteristics across various upstream water depths and flume outlet heights, categorized by distinct groups based on flow regimes. The experimental setup incorporates measurements of air-water mixture density, air cavity pressure, cavity water depth, and velocity profiles in the recirculation pool downstream of the weir. Results indicate that under supercritical downstream flow conditions, the forces exerted on the weir are directly proportional to the upstream water depth, while the downstream flume depth has a minimal impact. Conversely, in subcritical downstream conditions, the downstream flume depth significantly influences stabilizing forces due to increased cavity water depth. Additionally, pressure profile estimations on the downstream-facing wall of the weir using hydrostatic, Bernoulli, and Navier-Stokes equations show that the hydrostatic assumption is inadequate for estimating pressures and sliding forces in non-ventilated cavities. This study offers crucial insights into air-water flow dynamics in weirs, underscoring the importance of incorporating dynamic factors into weir design and hydraulic modeling.

ARTICLE HISTORY
Received 9 May 2024
Accepted 18 September 2024

KEYWORDS
Air-water flow; broad-crested weir; ventilated and non-ventilated cavity; discretized navier-stokes equation; experimental validation

1. Introduction

The effective management of vertical structures such as breakwaters, seawalls, and weirs is essential in safeguarding infrastructure and communities from extreme events like tsunamis and severe floods, often intensified by climate change. These phenomena pose significant risks, potentially destroying protective structures such as breakwaters and floodwalls, as evidenced by Hurricane Katrina (Seed et al. 2008), the 2004 Sumatra tsunami (Suppasri et al. 2012), the 2011 Tohoku tsunami (Bricker, Francis, and Nakayama 2012), and Typhoon Haiyan (Bricker et al. 2014). Specifically, the Tohoku event demonstrated the vulnerability of caisson breakwaters to sliding, foundation bearing capacity failure, and foundation scour (Arikawa et al. 2012; Bricker, Takagi, and Mitsui 2013; Jayaratne et al. 2014; Takagi 2015), while failures of gravity (T-wall, L-wall) and cantilever (I-wall) floodwalls were attributed to scour-induced overturning (Chock et al. 2013).

A critical factor in overflow scenarios is the sub-atmospheric pressure in the air cavity downstream of the vertical structure. Michel (1984) employed dimensional analysis to illustrate the relationship, termed as "air demand of the cavity," which correlates with ventilated cavity flow, air cavity pressure, and the structure's geometry. Laali and Michel (1984), Chanson (1996) demonstrated a linear relationship between cavity pressure and ventilated cavity flow, along with its correlation with the Froude number. Chanson (1996) further noted that air bubbles entrained along the cavity interface during a weir overfall lead to sub-atmospheric cavity pressure if external air supply is interrupted (Figure 1). This phenomenon is particularly evident on the leeward side of the structure, potentially increasing sliding forces and the likelihood of failure modes such as sliding, overturning, or punching. Experimental and computational fluid dynamics (CFD) simulations by Kim et al. (2022, 2024) and Zou et al. (2023) revealed negative cavity pressures and increased cavity water depth in the recirculation pool during overflow events. Similarly, Disanayaka Mudiyanselage (2017) and Patil et al. (2018) found that sub-atmospheric pressure within the cavity escalates the horizontal force acting on the weir, thus compromising structural stability during overflow.

Another important aspect in such scenarios is the air-water flow in the recirculation pool, induced by entrained air bubbles. This flow is pivotal in various hydraulic engineering and fluid mechanics

CONTACT Jeremy Bricker jeremydb@umich.edu

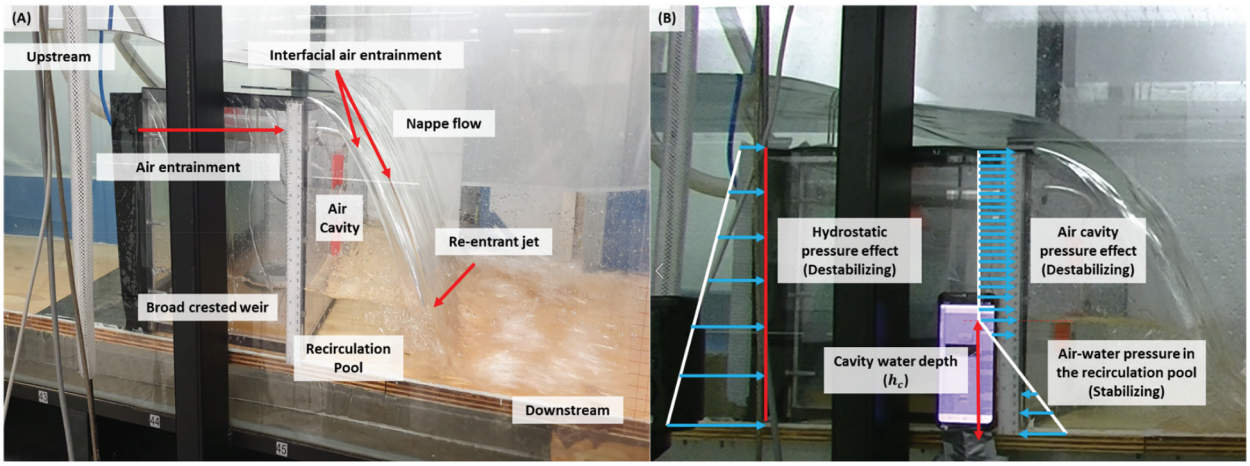

Figure 1. (a) air bubble entrainment along the cavity interface. (b) Illustration of the effects of air cavity pressure, cavity water depth, and air-water flow on forces affecting a broad-crested weir.

applications. From a hydraulic perspective, the design of hydraulic structures must consider the effects of ventilation: (1) The presence of air can cause flow bulking, which increases the depth of the flow mixture (Falvey 1980); (2) Introducing aeration near a structural bed can help mitigate the risk of cavitation (Koen, Bosman, and Basson 2019); and (3) air next to a solid boundary can reduce the drag (e.g. Air Cavity Ships (ACS)), which harness the principles of air-water flow, have been shown to reduce drag by 10–30% while only needing less than 2% additional power for air supply (Latorre 1997; Matveev, Burnett, and Ockfen 2009). Ventilating a cavity is effective in reducing flow instabilities, offering significant benefits in multiple engineering applications (Mäkiharju, Ganesh, and Ceccio 2017; Papillon et al. 2002).

In coastal engineering, especially in the design of vertical structures such as breakwaters, seawalls, and weirs, this air-water flow induced by jet impingement is crucial. This is because the void fraction or interfacial velocity of the air-water flow influences the forces acting on vertical structures: (1) The void fraction profile of air-water flow generated by nappe flow in a stepped chute varies based on the upstream discharge and the location of downstream jet impingement (Felder and Chanson 2015, 2017; Felder, Hohermuth, and Boes 2019). This profile can exhibit S-shaped or jet-like forms; thus, in situations of overflow, the density of the recirculation pool should incorporate air-water density considering void fraction. (2) The interfacial velocity on stepped spillways were closely correlated with a power law, which also depends on the discharge and the measurement location (Felder and Chanson 2015, 2017; Felder, Hohermuth, and Boes 2019). Moreover, the interfacial velocity resulting from air bubble movement acts on the face of vertical structure, generating additional hydrodynamic force beyond pressure.

Despite its importance, the properties of air-water flow are often overlooked in the current design of vertical structures in coastal engineering. Conventional design methods, such as the Goda formula established in 1972 for calculating wave forces (Goda 2010), typically do not include air-water flow properties. This formula, later refined by Tanimoto and Takahashi (1994) to incorporate additional factors, presumes a trapezoidal pressure distribution applicable for single-phase water flow. This limitation extends to the ASCE 7–16 guidelines, which are based on the extended Goda formula but do not consider air cavity pressure and air-water flow characteristics in the recirculation pool such as air-water density, interfacial velocity, and non-hydrostatic pressure profile. This trend persists in recent research. Yoshida et al. (2018) estimated the lift force and drag force exerted by concrete blocks for toe protection of mound breakwaters through experimentation and CFD simulation. However, air-water flow properties were not considered. Similarly, Hess, Boes, and Evers (2023) presented directional flow forces on vertical structures when subjected to impulse waves, dividing them into cases of wave run-up and overtopping. Yet, the air-water flow properties resulting from overtopping were also not accounted for.

Therefore, this study aims to determine the correct pressure profile on the structure face in the recirculation pool for ventilated and non-ventilated cavities, as this pressure profile is needed for calculation of the sliding force exerted on the structure by the water, as well as the punching pressure exerted by the structure on its foundation. In current design guidelines such as ASCE7, the pressure on both sides of the structure is assumed to be hydrostatic, as no other method exists to determine these pressures (American Society of Civil Engineers 2021). Three different approaches for calculating the

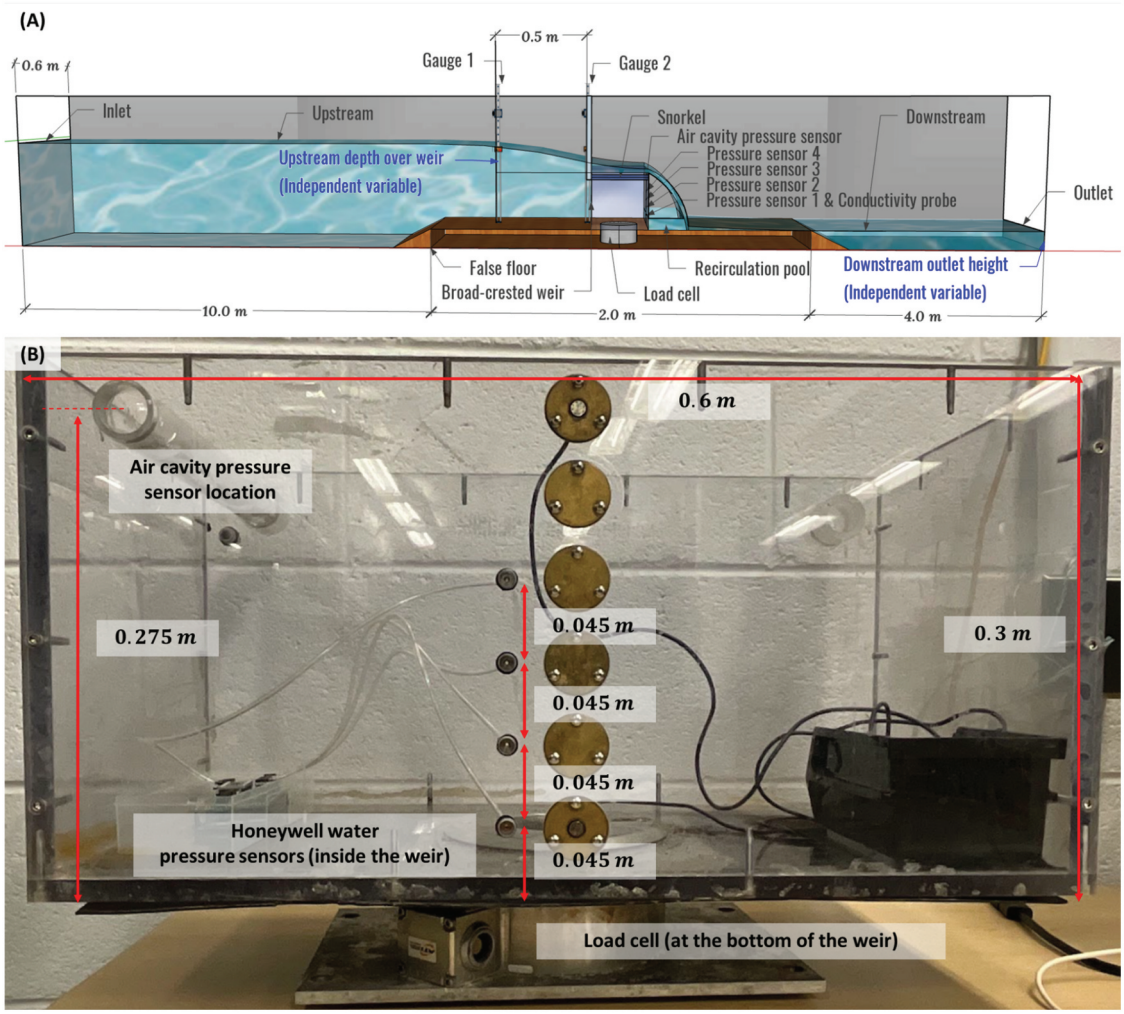

Figure 2. (a): experimental setup and sensor placement, with independent variables highlighted in blue, (b): downstream wall of the weir view, showing pressure sensors and loadcell placement.

pressure distribution in the recirculation pool are considered: 1) Hydrostatic, 2) Bernoulli equation, and 3) discretized Navier–Stokes equation. We compare each of these approximations against force and pressure data measured in the laboratory. The density of the air-water flow in front of the vertical wall is measured using a dual-tip conductivity probe, while flow velocity and turbulent viscosity are evaluated using Bubble Image Velocimetry (BIV). Additionally, the fluctuating cavity water depth is determined using the edge detection algorithm. The main focus of this research is to compute pressure profiles in the recirculation pool on the downstream wall of the overflowed structure under different assumptions and compare them with observed values, aiming to determine the most suitable assumption for the vertical variation of pressure in the recirculation pool. From this vertical pressure distribution, the horizontal destabilizing (sliding) force exerted by the water on the structure can be calculated for overflow events, thereby allowing confident formulation of design guidelines for vertical structures subject to overflow.

2. Methodology

2.1. Flume and model coastal structure

Figure 2 illustrates the experimental setup including the various instrumentation and the locations of measurements. Figure 2a shows the side view of the setup, including independent variables such as the upstream depth over the weir and the downstream outlet height. Figure 2b shows the downstream wall of the weir, indicating the locations of the pressure sensors. A GUNT HM 161 experimental flume was used in the study, with dimensions of 16 m length, 0.6 m width, and 0.8 m height. The upstream water depth was controlled by adjusting the flowrate using two parallel pumps. The flume's downstream outlet height is adjustable, allowing for control of downstream depth. In this experiment, the outlet height (h_o) was varied to 0.05, 0.10, 0.15, 0.20 m. As a small-scale representation of a coastal structure, a model cuboid-shaped broad-crested weir was constructed with length ($L_b = 0.3m$), width ($W_b = 0.6m$), and height ($h_b = 0.3m$). This weir matches the flume's width closely (1 mm gaps, water stopped by rubber diaphragms, are retained on the

sides and bottom of the box to allow load cell measurements). To measure downstream water pressure in the recirculation pool, four Honeywell Trustability Board Mount Pressure Sensors were installed inside the weir. Detailed specifications of all sensors are provided in the "Instrumentation specification and calibration" section. These sensors were placed at different elevations along the downstream side wall, ranging from 0.045 to 0.180 m from the bottom of the flume. A false floor was installed to affix a submersible load cell for measuring forces exerted on the weir. Flexible rubber diaphragms were inserted upstream of the gaps between flume walls and the model, as well as between the false floor and the model, to prevent water flow through the gaps, ensuring two-dimensional flow conditions.

For cavity ventilation, a PVC tubing snorkel with a diameter of 0.025 m and a length of 0.825 m was installed at a height of 0.275 m above the weir's bottom. In the ventilated case, this snorkel allowed external air supply into the cavity, while in the non-ventilated case, the tubing was closed to halt external air supply. An air pressure sensor was installed at the end of the PVC tubing snorkel to measure cavity pressure throughout the experiments. The measured air cavity pressure at this location was assumed to be representative of the entire cavity pressure.

2.2. Instrumentation and calibration

Table 1 represents the specifications of measurement instruments used in the experiments. A Load Cell (Omega160 IP68) measured force, offering a maximum horizontal force range of 2500 N with an accuracy of 1.75% of the full-scale range. Honeywell Trustability Board Mount Pressure Sensors assessed the air-water pressure in the recirculation pool, providing a range of 6894.6 Pa with an accuracy of 1% of the full-scale range. Air cavity pressure was measured using a "Dwyer Series 616KD Differential Pressure Transmitter," featuring a pressure range of 746.52 Pa with an accuracy of 2% of the full-scale range. A dual-tip conductivity probe from the UNSW Water Research Laboratory (Felder and Chanson 2017; Felder, Hohermuth, and Boes 2019) was used to detect bubbles and calculate the local void fraction needed to calculate the air-water density. The probe tips were positioned on the middle of the downstream face of the model, facing the bottom of the flume, situated 0.045 m above the false floor, ensuring their constant submersion within the recirculation pool for all experiments. A flexible arm, connecting the probe tips to the data acquisition hardware, was extended outside the flume through a PVC snorkel to avoid interference with the nappe flow. For upstream depth measurements, Edinburgh Designs WG8USB resistance-type Wave Gauges were utilized. In Figure 2, Gauge 1 (left gauge in the figure), located 0.5 m from the weir front wall, was used to measure the upstream depth over the weir (h_{up}). Gauge 2 (right gauge in the figure) was used to measure the water depth directly at the weir front wall (h_s), which was then used to calculate the hydrostatic force acting on the weir front wall. These wave gauges are calibrated by varying the water depth in the laboratory flume, resulting in an error rate of less than 0.1% of the full scale. Force data from the load cell, pressure data, and air fraction data from the conductivity probe were acquired using NI LabVIEW, while upstream depth data from the wave gauges were measured using Edinburgh Designs proprietary software. Data synchronization among all acquisition software was conducted using linear interpolation, and the final sample rate and sample duration were 10 hz and 30 s, respectively.

2.3. Independent variables

For a design flood, storm surge, or tsunami that a coastal or hydraulic structure of a given height is exposed to, a shallow water simulation can be used to determine the water depth upstream of the structure and the water depth downstream of the structure, so our analysis considers these to be independent variables. From these independent variables, designers need to calculate the force exerted on the structure. Experiments were conducted for 28 different cases with independent variables. The first independent variable, flume downstream outlet height (h_o) (refer to Figure 2), was categorized into four groups, as shown in Table 2. Groups 1 through 3 each consist of 8 cases, while the final Group 4 comprises 4 cases. Flume downstream outlet height plays a crucial role in

Table 1. Specifications of measurement instruments used in the experiments.

Instrument	Measurement Type	Range	Accuracy	Sample rate	Sample duration	Calibration
Load Cell (Omega160 IP68)	Directional force	2500 N	1.75%	10 hz	30 s	Calibrated
Honeywell Pressure Sensor	Air-water pressure	6894.8 Pa	1%	10 hz	30 s	Calibrated
Dwyer Series 616KD Differential Pressure Transmitter	Air cavity pressure	746.5 Pa	2%	10 hz	30 s	Calibrated
WRL Conductivity Probe	Local air concentration	0 or 1	<5%	20 kHz	30 s	Raw interface data
Edinburgh Designs WG8USB Wave Gauge Controller	Upstream depth	700 mm	<0.1%	125 hz	30 s	Calibrated

determining the downstream flow regime and was selected as the first independent variable due to its significance and ease of obtainability in real-word scenarios. Groups 1 to 2 exhibit relatively low-outlet heights, observed to have supercritical downstream conditions based on video observations, as depicted in Figure 3. Group 3 also displays supercritical downstream conditions; However, in comparison to Groups 1 and 2, Group 3 experienced a transition from supercritical to subcritical flow immediately after jet impingement due to the occurrence of a hydraulic jump. Group 4 features relatively high-outlet heights with subcritical downstream flows with similarity in the cavity water depth in the recirculation pool and the downstream water depth (there is no supercritical section or hydraulic jump).

The second independent variable is the upstream depth (h_{up}) relative to the weir crest (refer to Figure 2). Unlike the first variable, this variable does not have a fixed value. Instantaneous upstream depth is measured over time using a wave gauge. Each case within a group has a different average value, and Table 2 displays the range, including the minimum and maximum values of these averages.

The third independent variable is the ventilation of the cavity. In the ventilated case depicted in Figure 4, where external air is artificially supplied into the cavity, the air flow rate is non-zero. Conversely, in the non-ventilated case, where external air is not supplied, the air flow rate is zero.

2.4. Density measurement

The dual-tip conductivity probe, identical to the one used by Felder and Chanson (2015) and shown in Figure 2 was employed to measure the void fraction (C) within the recirculation pool. Observing air bubbles and water droplets at a fixed location within the air–water flows over a specific sampling duration constitutes the measurement of air–water interfaces in a Eulerian manner. At this location, air bubbles and water droplets are detected as they penetrate the probe tips, resulting in a voltage signal difference. By detecting voltage differences at air and water interfaces, the time-averaged local void fraction was calculated. Subsequently, the density of the air-water flow (ρ_m) was determined using the densities of air (ρ_a) and water (ρ_w) in Eq. (1) as follows:

$$\rho_m = \rho_a C + \rho_w (1 - C) \tag{1}$$

The density of the recirculation pool near the downstream face of the weir was determined by measuring the void fraction throughout the duration of the experiment. Instantaneous void fraction measurements were converted to instantaneous air-water density using Eq. (1). An instantaneous voltage exceeding 4 V indicated the presence of the water phase, while a voltage below 0.5 V indicated the presence of the air phase. Consistently throughout the experiment, the voltage remained above 4 V, indicating that the probe consistently measured the water phase. This process was repeated for all experimental cases, and near the weir wall, the voltage consistently exceeded 4 V, indicating that in all cases, the region is in the water phase. Therefore, the void fraction is equal to 0 and water density can be regarded as air-water density in these conditions ($\rho_m = \rho_w$). This finding is consistent with the movement of air bubbles in the recirculation pool as illustrated in Figures 3 and 4, where there was no air at all in front of the downstream weir wall.

2.5. Velocity measurement

Bubble Image Velocimetry (BIV), introduced by Ryu, Chang, and Lim (2005) was employed to determine the velocity field in the recirculation pool beneath the cavity, as indicated by the camera marker in Figure 4(a). The process involved capturing high-frame-rate footage at 1920 × 1080 pixels and 120 hz using a Sony-ZV1 camera. The analysis was conducted using the PIVlab MATLAB toolbox (Stamhuis and Thielicke 2014; Thielicke 2014; Thielicke and Sonntag 2021). It calculates velocity vectors through cross-correlation, estimating the displacement of bubbles between consecutive frames. The velocity v is determined using the equation: $v = \frac{\Delta x}{\Delta t}$. Here, Δx is the displacement of a bubble between images, and Δt is the time interval between frames. Figure 5 depicts the setup utilized in this study for BIV analysis. The original plot includes measurements obtained from the camera, with the PC time recorded simultaneously to aid in data synchronization with the velocity data acquired from BIV. A ruler was captured within each frame for length calibration purposes, and the velocity field

Table 2. Experimental conditions and independent variables overview.

Groups	Cases	Flume outlet height h_o [m]	Downstream regime	Upstream depth over weir h_{up} [m]	
				Ventilated	Non-ventilated
Group 1	01 ~ 08	0.05	Supercritical	0.064 – 0.104	0.065 – 0.103
Group 2	09 ~ 16	0.10	Supercritical	0.059 – 0.095	0.061 – 0.096
Group 3	17 ~ 24	0.15	Supercritical	0.086 – 0.144	0.090 – 0.147
Group 4	25 ~ 28	0.20	Subcritical	0.099 – 0.124	0.110 – 0.139

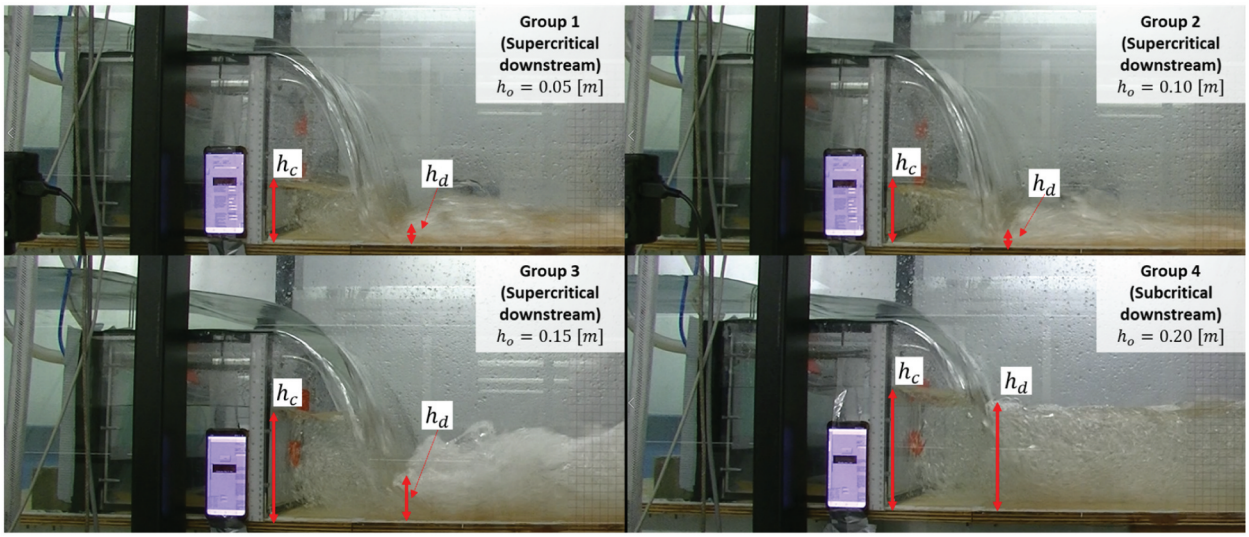

Figure 3. Downstream flow regime observations for different outlet height groups for the non-ventilated cases (h_c: cavity water depth, h_d: downstream depth).

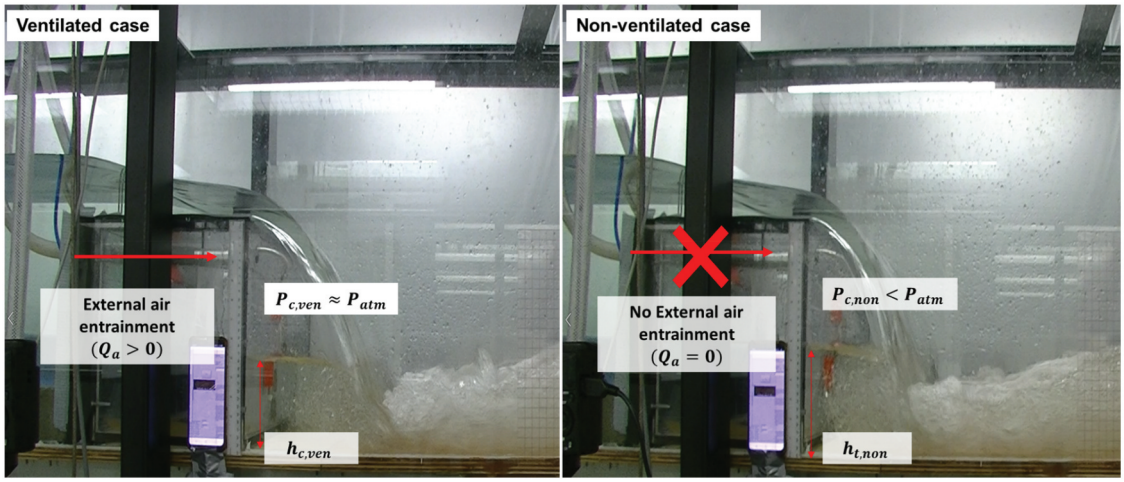

Figure 4. Comparison of air flowrate in the ventilated and non-ventilated cases.

within the Region of Interest (ROI) highlighted by the blue rectangle is computed through analysis.

2.6. Eddy viscosity estimation

The concept of eddy viscosity was first introduced by Ludwig Prandtl in 1925, who posited that in turbulent flow, viscosity could be considered a fluctuating quantity, varying in both time and space. Prandtl also developed the mixing length theory, linking eddy viscosity to the turbulence's characteristic length scale. The eddy viscosity v_t can be estimated using the formula: $v_t = l_m^2 \frac{du}{dy}$ (Prandtl 1925). Here, l_m is the mixing length, and $\frac{du}{dy}$ is the velocity gradient perpendicular to the wall.

In this experiment, eddy viscosity was estimated within the available experimental setup by assuming a logarithmic layer. In the logarithmic layer, the mixing length l_m is typically proportional to the distance from the wall, represented as $l_m = \kappa y$, as suggested by (Galbraith and Head 1975). This proportionality can be represented using the von Kármán constant (κ), approximately 0.41 for most turbulent boundary layers. The mixing length is then expressed: $l_m = \kappa y$. Incorporating this into Prandtl's formula results in the equation for estimating eddy viscosity: $v_t = \kappa^2 y^2 \frac{du}{dy}$ where y is the wall distance.

2.7. Cavity water depth measurement

For cavity water depth (h_t) measurements in the recirculation pool, the Canny edge detection method (Canny 1986), was applied for non-intrusive fluctuating water depth calculation. Since brightness is more important than color in the edge detection method, pre-processing was conducted on grayscale images to

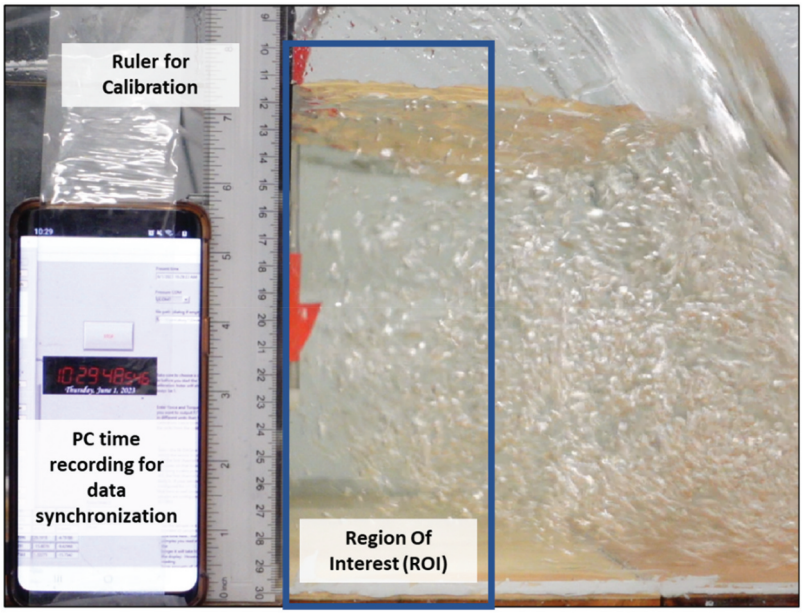

Figure 5. Experimental setup for bubble image velocimetry (BIV) analysis.

simplify the calculations. Calibration was performed similarly to the BIV used for velocity measurement, using real distances within the image captured by the camera.

2.8. Force measurement

The Omega 160 IP68 6-DoF load cell utilized in this experiment was installed beneath the broad-crested weir, as depicted in Figure 2, using a false floor. Capable of measuring both force and torque in all three dimensions, the load cell was used to capture data on the force exerted in the direction of flow for this experiment. To prevent any forces other than those acting on the weir from affecting the measurements, a gap of approximately 1 mm was maintained between the weir and the flume walls, as well as between the weir and the false floor. This gap was sealed with a rubber diaphragm to prevent friction.

2.9. Air-water pressure estimation

2.9.1. Governing equation

To develop an analytical estimation of the air-water pressure acting on the broad-crested weir, the two-dimensional, incompressible, vertical (y) directional momentum equation (Eq. (2)) is used for the governing equation in the research.

$$\frac{\partial v}{\partial t} + u\frac{\partial v}{\partial x} + v\frac{\partial v}{\partial y} = -\frac{1}{\rho_m}\frac{\partial p}{\partial y} + \nu_t\left(\frac{\partial^2 v}{\partial x^2} + \frac{\partial^2 v}{\partial y^2}\right) - g \quad (2)$$

Here, the parameter (u, v) represents the x (horizontal, positive rightward) and y (vertical, positive upward) directional velocities in the recirculation pool, ρ_m is the density in the recirculation pool, ν_t is the eddy viscosity in the recirculation pool, and p is the pressure in the recirculation pool.

2.9.2. Domain

Figure 6 illustrates the temporal and spatial domain, utilizing a uniformly spaced spatial grid that is the same (x, y) grid used in the BIV to calculate the velocity vector field. The toe of the weir is set as the origin as shown in the left image of Figure 6. With the Sony-ZV1 camera's frame rate set at 120 frames per second, a corresponding time step of 1/120 seconds was chosen. In the temporal domain, the index "n" is utilized, while in the spatial domain, indices "i" and "j" represent the x and y directions, respectively. Thus, the notation $p_{i,j}^{n}$ represents the pressure at a specific time step indexed by "n" and spatial indices (i, j) within the domain. Similarly, the notation $v_{i,j}^{n+1}$ represents the velocity at the "$n + 1$" time step and spatial indices (i, j).

2.9.3. Pressure measurements at sensor locations

Air-water pressure measurements were obtained using sensors installed at elevations of $y = 0.045, 0.090, 0.135$, and 0.180 m. The pressure values at other locations are determined either by applying the Bernoulli equation or by numerically solving the discretized Navier–Stokes equation, incorporating the measured data.

2.9.4. Approach 1: hydrostatic assumption

Utilizing the hydrostatic assumption to estimate air-water pressure in the recirculation pool is the simplest and commonly used method in previous studies (American Society of Civil Engineers 2021). In this research, it serves as a rudimentary tool for comparison with air-water pressure obtained from the Bernoulli equation and the Discretized Navier–Stokes equation.

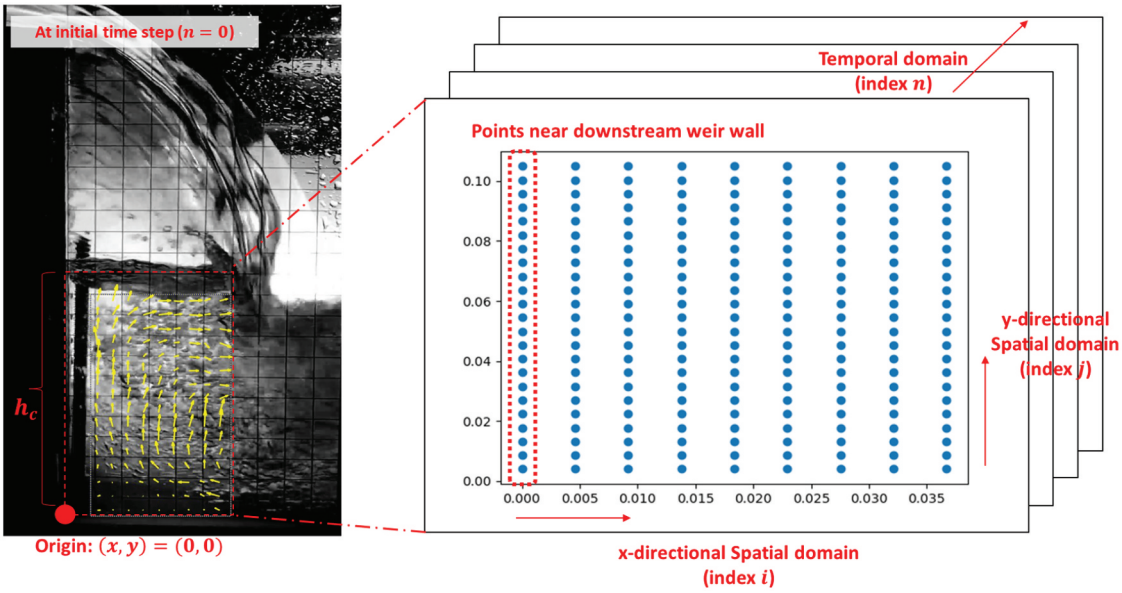

Figure 6. Temporal and spatial domain in the experiment for discretized Navier-Stokes equation.

The vertical momentum equation Eq. (2) is simplified to Eq. (3) under the assumptions of steady, uniform, and inviscid flow:

$$\frac{1}{\rho_m}\frac{\partial p}{\partial y} = -g \tag{3}$$

Considering the coordinate system and origin of the spatial domain in Figure 6, integrating Eq. (3) from the free water surface ($y = h_c$) to a depth y_h ($y = h_c - y_h$) below allows for the estimation of hydrostatic pressure, denoted as p_h.

$$p_h = p_c + \int_{y=h_c}^{y=h_c-y_h} -\rho_m g dy = p_c + \rho_m g y_h (0 \le y_h \le h_c) \tag{4}$$

Here, p_c represents the air cavity pressure, which is obtained from pressure sensor, and h_c is the cavity water depth, which is not a constant value but is obtained from the edge detection method used in image processing and varies in time. For the ventilated case, the air cavity pressure is zero, while for the non-ventilated or partially ventilated case, the air cavity pressure is less than atmospheric pressure.

2.9.5. Approach 2: Bernoulli equation

The second method employed for estimating air-water pressure in the recirculation pool involves the utilization of Bernoulli's equation. Unlike the first approach, which relies on the hydrostatic assumption, this method incorporates the consideration of velocity-induced dynamic pressure. Under the assumptions of steady and inviscid flow, Eq. (2) is simplified to Eq. (5).

$$\vec{v} \cdot \nabla \vec{v} = -\frac{1}{\rho_m}\frac{\partial p}{\partial y} - g \tag{5}$$

Rearranging all terms to the left-hand side and integrating, Eq. (5) results in:

$$p + \tfrac{1}{2}\rho_m \vec{v}^2 + \rho_m g y_h = constant \tag{6}$$

In Eq. (6), p is the static pressure, $\frac{1}{2}\rho_m \vec{v}^2$ is the dynamic pressure, representing the kinetic energy per unit volume, and $\rho_m g y_h$ is the potential energy per unit volume. The dynamic pressure is obtained from the BIV measurement at each elevation y_h which also defines potential energy. The static pressure term (p) is initially measured at a pressure sensor location, and the total head is calculated at this location and subsequently used to calculate the static pressure at other locations along the vertical direction near the downstream weir wall within the cavity water. This method assumes ideal, frictionless flow, for which the total pressure is constant along a streamline.

2.9.6. Approach 3: discretized Navier-Stokes equation

While Bernoulli's equation proves to be a valuable and widely applied tool for addressing simple fluid flow problems, it has a limitation in that it does not consider viscosity. On the other hand, the Navier–Stokes equations are highly versatile, capable of modeling various fluid flows encompassing turbulence, viscosity, and compressibility. However, their complexity makes obtaining analytical solutions difficult, often necessitating significant computational resources for numerical solutions. However, in this experiment, since all data except for air-water pressure is obtained through measurements at every point within the domain in advance, and air-water pressure readings were also obtained from water pressure sensors installed at elevations of $y =$ 0.045, 0.090, 0.135, and 0.180 m, no complex

methods are required to estimate air-water pressure at other elevations within the domain. Instead, a simple Finite Difference Method, utilizing Forward/Backward difference, is employed to discretize the Navier–Stokes equation.

3. Boundary conditions

In this research, velocity values were known at every point within the time and spatial domain, via measurement with BIV. The Navier Stokes equation was used to calculate the spatial distribution of pressure. For pressure boundary conditions, the measured pressure value at $y = 0.045m$ obtained from pressure sensor, which is Dirichlet boundary condition is used. Since the pressure term in the Navier Stokes equation is first order in space, one boundary condition (or measurement) is needed.

4. Discretization schemes and equations

The pressure at various points within the domain is computed using discretization schemes, employing the Forward Euler method for the time derivative and either forward or backward difference for spatial derivatives. Specifically, the backward difference scheme in the y-direction is employed for y values greater than the pressure sensor elevation of 0.045 [m], while the forward difference scheme is utilized for y values less than this elevation. Table 3 provides the resulting discretized equations for each differential term. These discretized terms are then substituted into the Navier–Stokes equation (Eq. (2)) to derive the discretized Navier–Stokes equation. By substituting measurements into this equation, the air-water pressure is calculated.

4.1. Sliding force calculation

The sliding force acting on the broad crested weir model during overflow varies between the ventilated and non-ventilated cases. For the upstream side, the water pressure force at the upstream face (F_u) of the weir is calculated using the hydrostatic assumption as shown in Eq. (7):

$$F_u = \frac{1}{2} h_b(\rho_w g h_s + \rho_w g(h_s - h_b))W_b \tag{7}$$

where h_b is the weir height, ρ_w is the density of water, h_s is the water depth at the upstream face of the weir (measured from Gauge 2), and W_b is the weir width. However, on the downstream wall of the weir, as depicted in Figure 1b, the force is composed of two components: the stabilizing force due to cavity water depth and the destabilizing force due to air cavity pressure. Consequently, the calculation methods differ between the ventilated and non-ventilated cases. The stabilizing force at the downstream wall $(F_s)_d$ is derived by integrating the air-water pressure profile over the cavity water depth. Here, $\Delta y = y_{j+1} - y_j$ is the vertical distance between adjacent points.

$$(F_s)_d = \left[\int_{y=0}^{y=h_t} p(x,y)dy\right] W_b = \sum\left(\frac{p_{i,j}+p_{i,j+1}}{2}\right)\Delta y W_b \tag{8a}$$

Equation (8a) relies on discrete pressure estimates, denoted as $p_{i,j}$, along the model's downstream face. These values are obtained from each of the pressure profiles (Hydrostatic condition, Bernoulli equation or the discretized Navier–Stokes equation).

For the destabilizing force on the downstream face $(F_d)_d$, it is assumed that the air cavity pressure (p_c) is constant throughout the entire air cavity. Thus, the destabilizing force can be calculated as shown in Eq. (8b), where h_b is the weir height, h_c is the cavity water depth, p_c is the cavity pressure, and W_b is the weir width. This force is negative because the air cavity pressure is less than atmospheric

Table 3. Discretized schemes and equations for Navier–Stokes equation.

Terms	Discretization scheme	Discretized equation	Order of accuracy
$\frac{\partial v}{\partial t}$	Forward Euler	$\frac{v_{i,j}^{n+1} - v_{i,j}^{n}}{\Delta t}$	1
$\frac{\partial v}{\partial x}$	Forward difference	$\frac{v_{i+1,j}^{n} - v_{i,j}^{n}}{\Delta x}$	1
$\frac{\partial v}{\partial y}$	Forward difference (When $y > 0.045[m]$)	$\frac{v_{i,j+1}^{n} - v_{i,j}^{n}}{\Delta y}$	1
	Backward difference (When $y < 0.045[m]$)	$\frac{v_{i,j}^{n} - v_{i,j-1}^{n}}{\Delta y}$	
$\frac{\partial p}{\partial y}$	Forward difference (When $y > 0.045[m]$)	$\frac{p_{i,j+1}^{n} - p_{i,j}^{n}}{\Delta y}$	1
	Backward difference (When $y < 0.045[m]$)	$\frac{p_{i,j}^{n} - p_{i,j-1}^{n}}{\Delta y}$	
$\frac{\partial^2 v}{\partial x^2}$	Forward difference	$\frac{-v_{i+3,j}^{n} + 4v_{i+2,j}^{n} - 5v_{i+1,j}^{n} + 2v_{i,j}^{n}}{\Delta x^2}$	2
$\frac{\partial^2 v}{\partial y^2}$	Forward difference (When $y > 0.045[m]$)	$\frac{-v_{i,j+3}^{n} + 4v_{i,j+2}^{n} - 5v_{i,j+1}^{n} + 2v_{i,j}^{n}}{\Delta y^2}$	2
	Backward difference (When $y < 0.045[m]$)	$\frac{-v_{i,j-3}^{n} + 4v_{i,j-2}^{n} - 5v_{i,j-1}^{n} + 2v_{i,j}^{n}}{\Delta y^2}$	

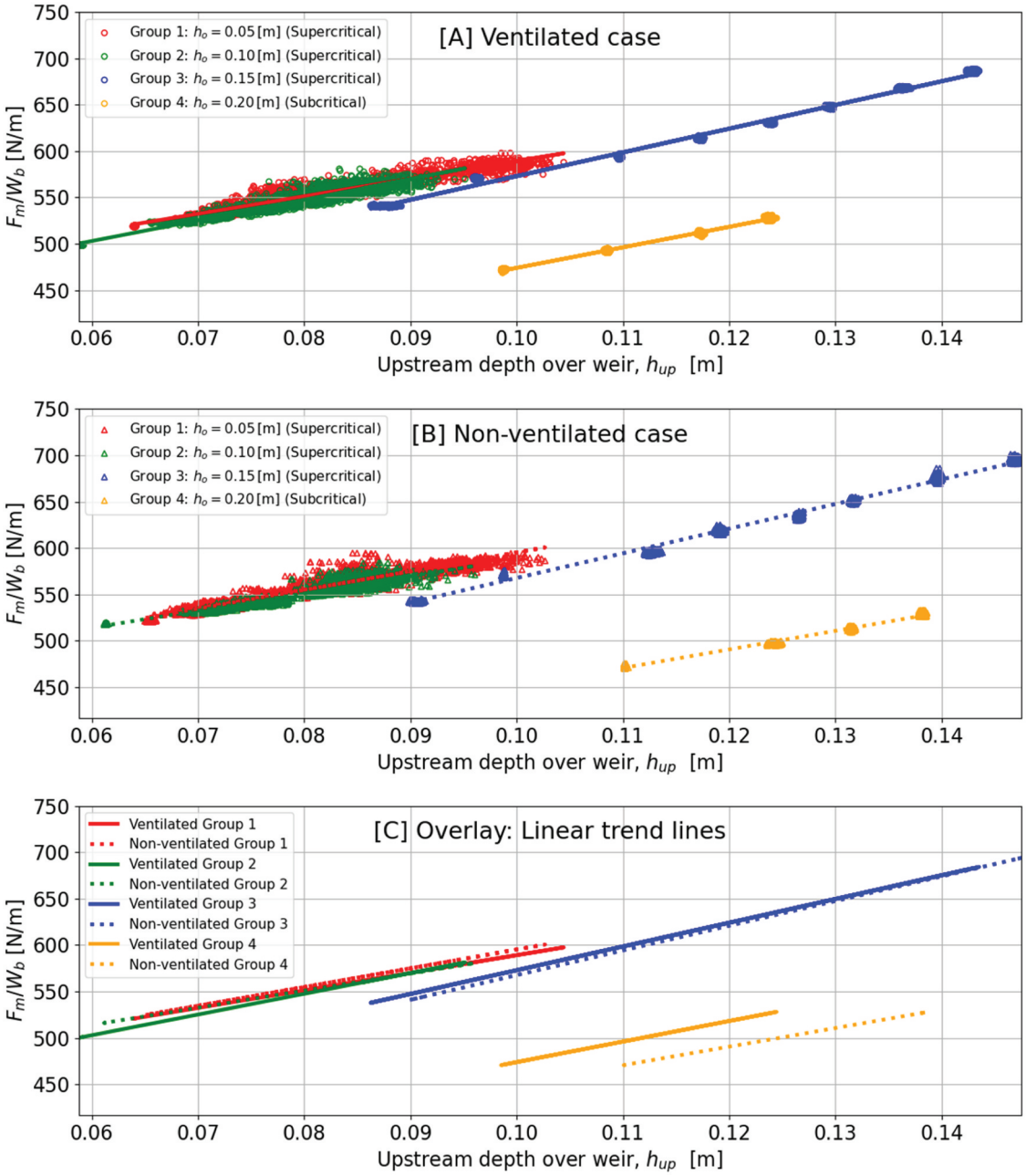

Figure 7. Scatter plot of instantaneous measured force for each experimental group: (a) the ventilated case, (b) the Non-ventilated case, (c) trend lines for both cases.

pressure, resulting in negative gauge pressure in the non-ventilated cavity.

$$(F_d)_d = (h_b - h_c)p_c W_b \tag{8b}$$

Then, the calculated total sliding force F_c in both the ventilated and non-ventilated cases is calculated using Eq. (9) by subtracting downstream forces from upstream force, considering the direction of the forces.

$$F_c = \left\{\tfrac{1}{2}\rho_w g h_b(2h_s - h_b) - \left[\sum\left(\tfrac{p_{ij}+p_{ij+1}}{2}\right)\Delta y + (h_b - h_c)p_c\right]\right\}W_b \tag{9}$$

This equation is valid for both ventilated and non-ventilated conditions, with the appropriate air cavity pressure value (0 for fully ventilated, sub-atmospheric for partially ventilated or non-ventilated).

5. Results

5.1. Measured forces and flow characteristics

The data in Figure 7 provide a comprehensive analysis of the measured forces per unit width (F_m/W_b) on a weir across various upstream water depths (h_{up}) for both ventilated and non-ventilated conditions, segmented into four groups based on flume outlet heights (h_o). Figure 7a,b illustrate the instantaneous measured force for each group, with circle markers for ventilated cases and triangle markers for non-ventilated cases. Groups 1 and 2 (red and green) exhibit a continuous range of upstream depths. Conversely, Groups 3 and 4 (blue and orange) display a finite number of discrete upstream depths. This difference is related to the

stability of the pump supplying the flow. For Groups 1 and 2, the pump speed was operated with a slow, continuous increase, resulting in a continuous range of upstream depths being used in the experiments. In contrast, for Groups 3 and 4, the pump speed was set to constant, discrete values, leading to a finite number of discrete upstream depth values. Despite these differences in upstream depth ranges, the accuracy of the analysis is not compromised because the study uses instantaneous data. Each relevant variable is measured concurrently with the upstream depth, ensuring the reliability of the results. Figure 7c compares data from Figure 7a,b with trend lines, using solid lines for ventilated cases and dashed lines for non-ventilated cases.

One observation from Figure 7c is that the force acting on the weir linearly varies with upstream depth over the weir, regardless of the ventilation condition. Particularly in supercritical conditions (Groups 1 and 2), the measured force shows a linear dependence on the upstream depth, independent of the flume outlet height. In nearly critical (Group 3) and subcritical conditions (Group 4), the force still exhibits a linear relationship with upstream depth but shows lower overall values compared to Groups 1 and 2. This is because the subcritical condition, with increased outlet height, augments the stabilizing force on the box by increasing the cavity water depth. Another interesting observation from Figure 7c is the effect of flume outlet depth on cavity ventilation and its influence on sliding force. Previous studies by Disanayaka Mudiyanselage (2017) and Patil et al. (2018) indicated that the sliding force measured in non-ventilated cases was always greater than in ventilated cases. However, in this experiment, comparing the trend lines for ventilated and non-ventilated cases shows that, while the non-ventilated case has a higher measured force in Groups 1 and 2, the ventilated case has a higher force in Groups 3 and 4. This difference arises because, in Groups 1 and 2 (fully supercritical, $Fr \gg 1$), the increase in air cavity pressure (which increases sliding force) in non-ventilated cases outweighs the increase in cavity water depth (which reduces sliding force). Conversely, in Groups 3 and 4 ($Fr \approx 1$ or $Fr < 1$), the increase in air cavity water depth in non-ventilated cases outweighs the increase in cavity pressure, resulting in a lower sliding force compared to ventilated cases. The comparison and analysis of air cavity pressure and cavity water depth are explained in detail in the next section.

5.2. Assessing the dynamics of air-water flow: an empirical study of flow characteristics

To compute the forces acting on the weir using different downstream pressure profiles, measurements of air cavity pressure, cavity water depth, velocity profile in the recirculation pool, and air-water density must be conducted.

5.2.1. Air cavity pressure measurement results

Figure 8a illustrates the observed relationship between upstream depth over the weir and the measured negative air cavity pressure under ventilated conditions. Contrary to theoretical expectations that air cavity pressure in fully ventilated conditions should be zero, the experimental results show that when the upstream depth over the weir is 0.1 m or less, the air cavity pressure is 0 Pa as expected. However, when the upstream depth exceeds 0.1 m, the air cavity pressure becomes negative and increases quadratically with the upstream depth (Solid lines in Figure 8c). This suggests that the conditions in this study are not fully ventilated but rather partially ventilated for Groups 3 and 4. Another notable feature is that in the supercritical flow states (Groups 1 to 3), the negative air cavity pressures lie on the same trend lines, regardless of the flume outlet height. However, the influence of outlet height becomes significant when comparing Group 3 with Group 4, as the downstream flow transitions from supercritical to subcritical states. A marked decrease in negative air cavity pressure is observed in Group 4 compared to Group 3, indicating that subcritical conditions lead to a reduced development of negative air cavity pressure.

In Figure 8b, which focuses on non-ventilated conditions, a distinctive behavior of negative air cavity pressure is observed across Groups 1 to 3. Unlike the ventilated scenario, the negative air cavity pressure under non-ventilated conditions remains relatively constant and negative up to an upstream depth of approximately 0.11 m, beyond which it exhibits a steep quadratic increase in negativity. This indicates that, in the non-ventilated state, the air cavity pressure is initially less sensitive to changes in upstream depth but reacts more dramatically as the depth surpasses a threshold. In Group 4, under non-ventilated conditions representing subcritical flow, the air cavity pressure shows a unique pattern, deviating from the one observed in Group 3 yet still being influenced by the outlet height. Contrary to the partially ventilated condition where cavity pressure consistently remains lower than that of Group 3, the non-ventilated condition for Group 4 maintains a relatively constant negative pressure around −100 Pa up to an upstream depth of approximately 0.13 m. This pressure is notably higher than that measured for Group 3. However, as the upstream depth increases beyond 0.13 m, a shift occurs where the air cavity pressure in Group 4 starts to drop below that of Group 3, resembling the trend seen in the partially ventilated condition.

5.2.2. Cavity water depth measurement results

Figure 9 depict a linear correlation between the measured cavity water depth and the upstream depth over the weir, a trend that persists in both ventilated and non-ventilated conditions. In the ventilated

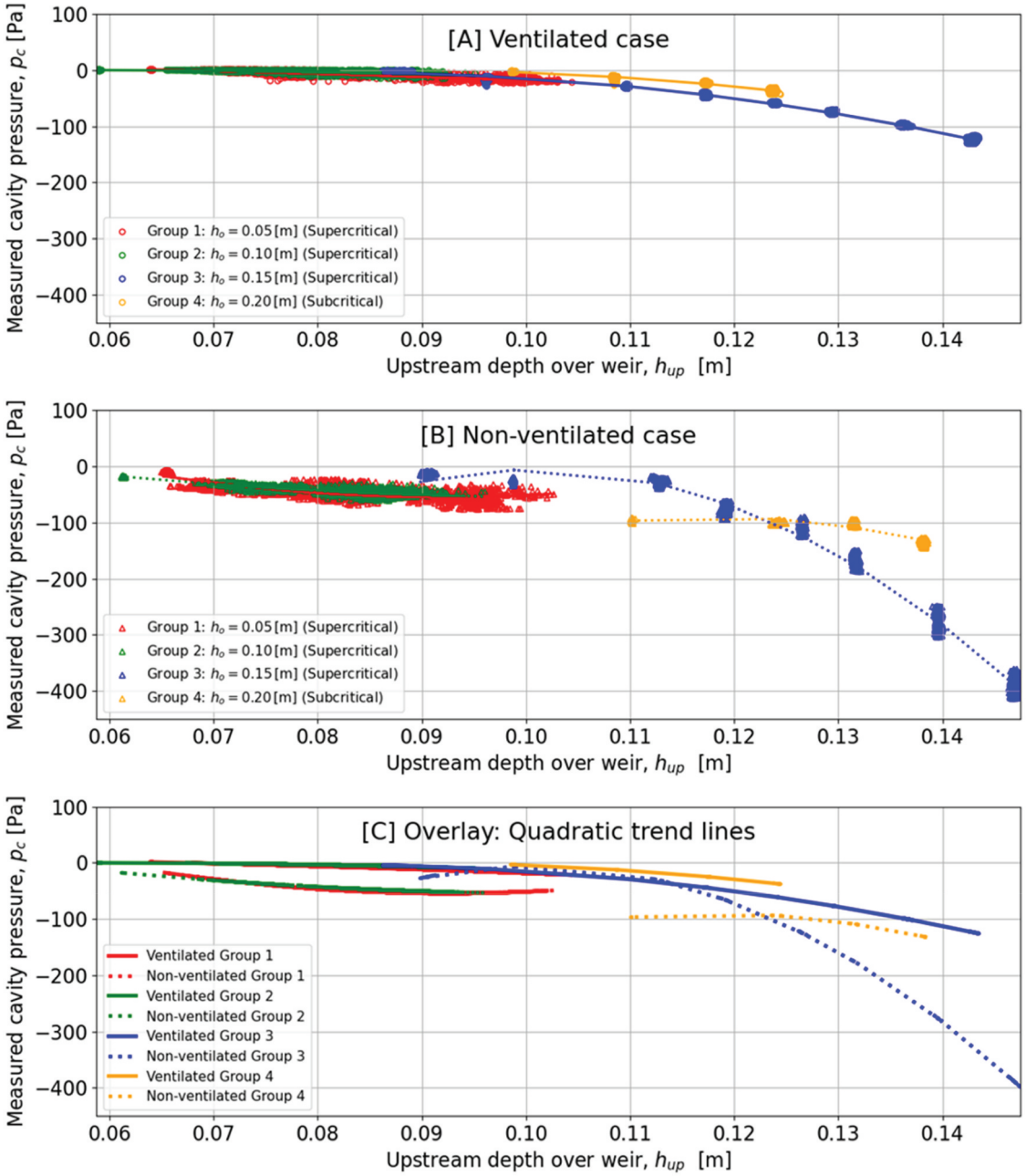

Figure 8. Scatter plot of measured cavity pressure vs. upstream depth over weir for different groups under (a) ventilated case, (b) Non-ventilated case, (c) trend lines for both cases.

scenario of Figure 9a, Groups 1 to 3, depicted in red, green, and blue, and operating with supercritical downstream flow regimes, display a proportional increase in cavity water depth with increasing upstream depth. This linearity aligns with the hydraulic principles governing supercritical flows, where upstream conditions directly influence cavity water depth. Conversely, Figure 9b illustrates that in non-ventilated conditions, there is a noticeable increase in cavity water depth for all groups relative to their ventilated equivalents. The higher cavity water depths signify a modified flow resistance, a direct consequence of eliminating ventilation, which manifests as increased cavity water depths for given upstream depths.

Group 4, visualized in orange and situated within a subcritical flow regime, exhibits a linear relationship between cavity water and upstream depths in both ventilated and non-ventilated cavity, yet the cavity water depths are significantly elevated compared to the supercritical groups. This heightened cavity water depth in Group 4 arises as the downstream flow transitions to subcritical, leading to a condition where the outlet height assumes a controlling influence over the cavity water depth.

5.2.3. *Velocity vector in the recirculation pool measurement results*

The selected Bubble Image Velocimetry (BIV) results are strategically showcased to emphasize the significant

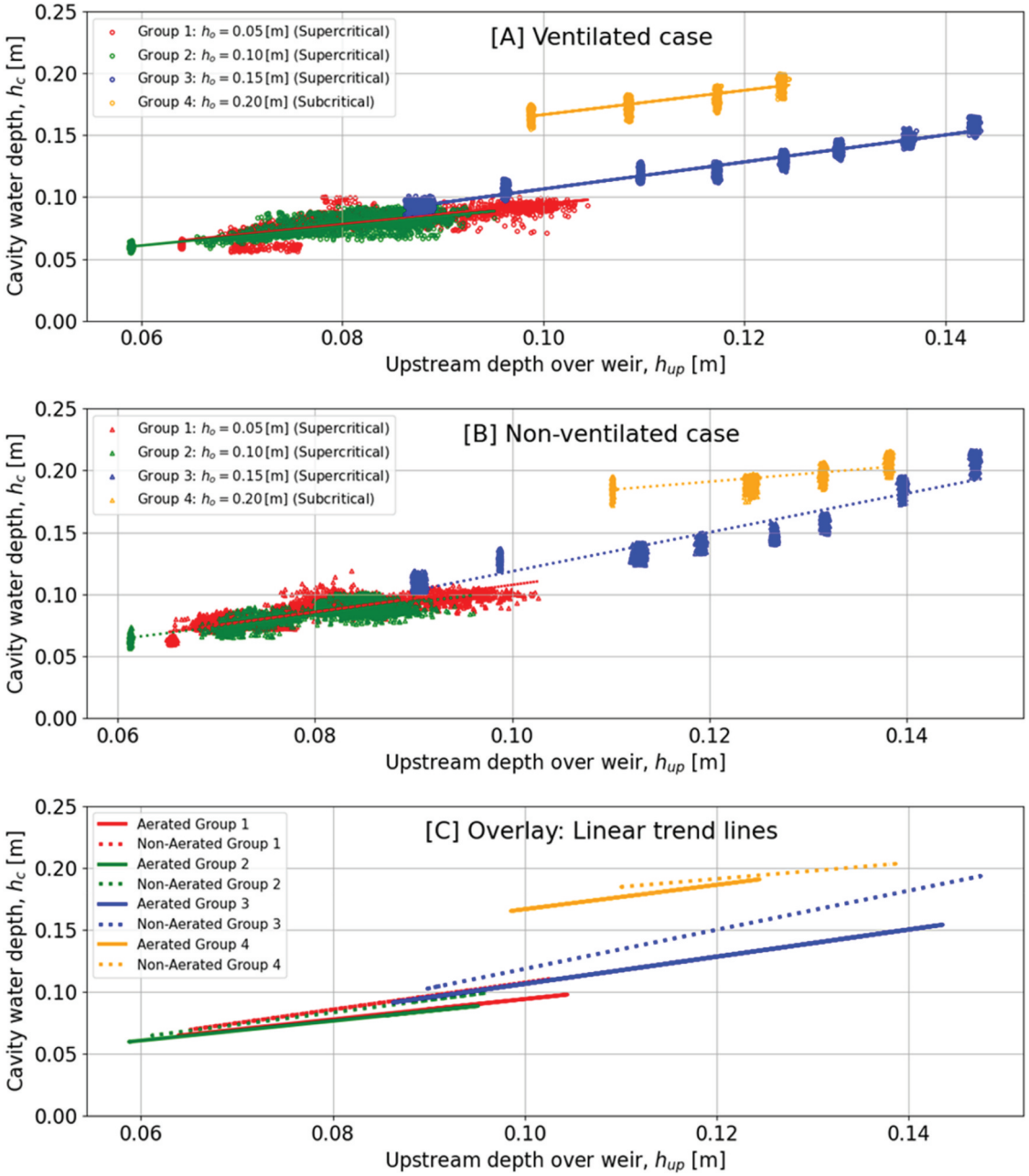

Figure 9. Scatter plot of measured cavity water depth vs. upstream depth over weir for different groups under (a) ventilated case, (b) Non-ventilated case, (c) trend lines for both cases.

influence of air bubble motion on the velocity vector field within the recirculation pool under contrasting ventilated and non-ventilated conditions. The observations drawn from Figure 10a,b demonstrate the BIV results for Group 1 to Group 4 with each ventilation condition. In these figures, the origin, as indicated in Figure 6, represents the toe of the weir, and the magnitude and direction of the time-averaged velocity vector are shown by the length and direction of the arrows. To better illustrate the time-averaged velocity magnitude, a colormap is also utilized, with blue indicating lower velocity magnitudes and red indicating higher velocity magnitudes. When examining the non-ventilated condition, as seen in Figure 10b, there is a noticeable increase in the velocity magnitude compared to Figure 10a, which is the ventilated condition. This suggests that the active movement of air bubbles in the recirculation pool under the non-ventilated condition significantly contributes to the increased velocity magnitude of the flow. This phenomenon occurs consistently across Groups 1 to 4, indicating that regardless of whether the downstream regime of the flume is subcritical or supercritical, the non-ventilated case exhibits more air bubble movement within the recirculation pool, leading to an increase in velocity magnitude. Examining the upper value of the colorbar in Figure 10 reveals that non-ventilated conditions induce a higher time-averaged velocity magnitude relative to their ventilated counterparts for Groups 1 to 3, which represent the supercritical downstream condition. For Group 4, the subcritical

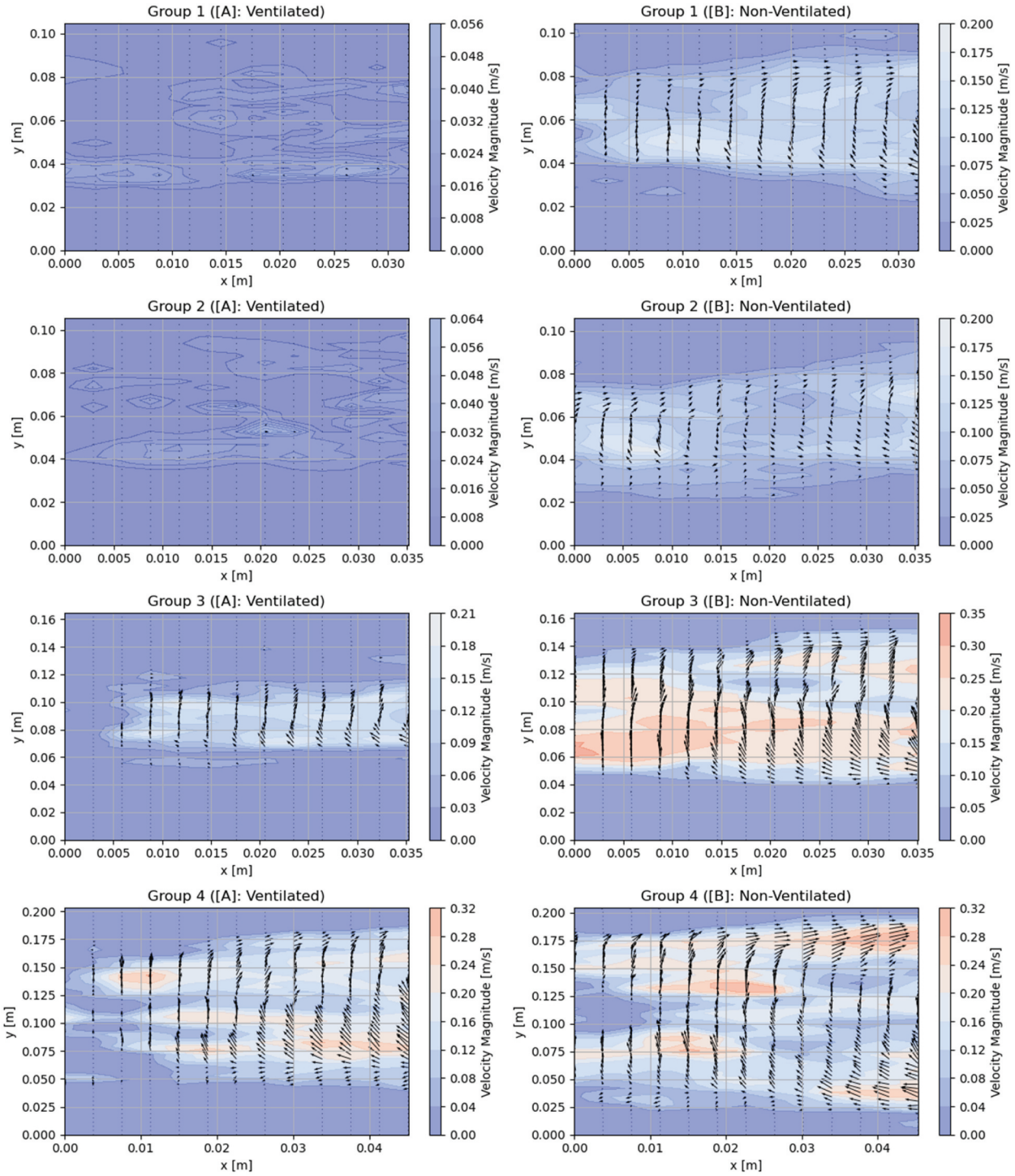

Figure 10. Impact of cavity ventilation on velocity vector fields in recirculation pools: BIV analysis for group 1 to group 4 (a: ventilated, b: non-ventilated). Colorbar represent the time-averaged velocity magnitude $[m/s]$.

downstream condition, while the upper value of the velocity magnitude (colorbar) is the same for both cases, the non-ventilated case shows a broader range with higher velocity magnitudes compared to the ventilated case. Notably, near the downstream wall of the weir at $x = 0$, the velocity magnitude in the non-ventilated case is significantly higher than in the ventilated case, similar to the supercritical case. Therefore, the velocity resulting from air-bubble movement in the non-ventilated case must be considered in force calculations.

5.3. Comparison of measured forces with those estimated using different pressure profiles

In this analysis, the comparison is made between the calculated forces derived from Eq. (9) with measurements and the measured force. The calculated force is obtained from three distinct pressure profiles: 1) Hydrostatic (Red color), 2) Bernoulli equation (Green color), and 3) Discretized Navier–Stokes equation (Blue color). Figure 11 represents the data and linear regression curve with the x-axis denoting the measured force

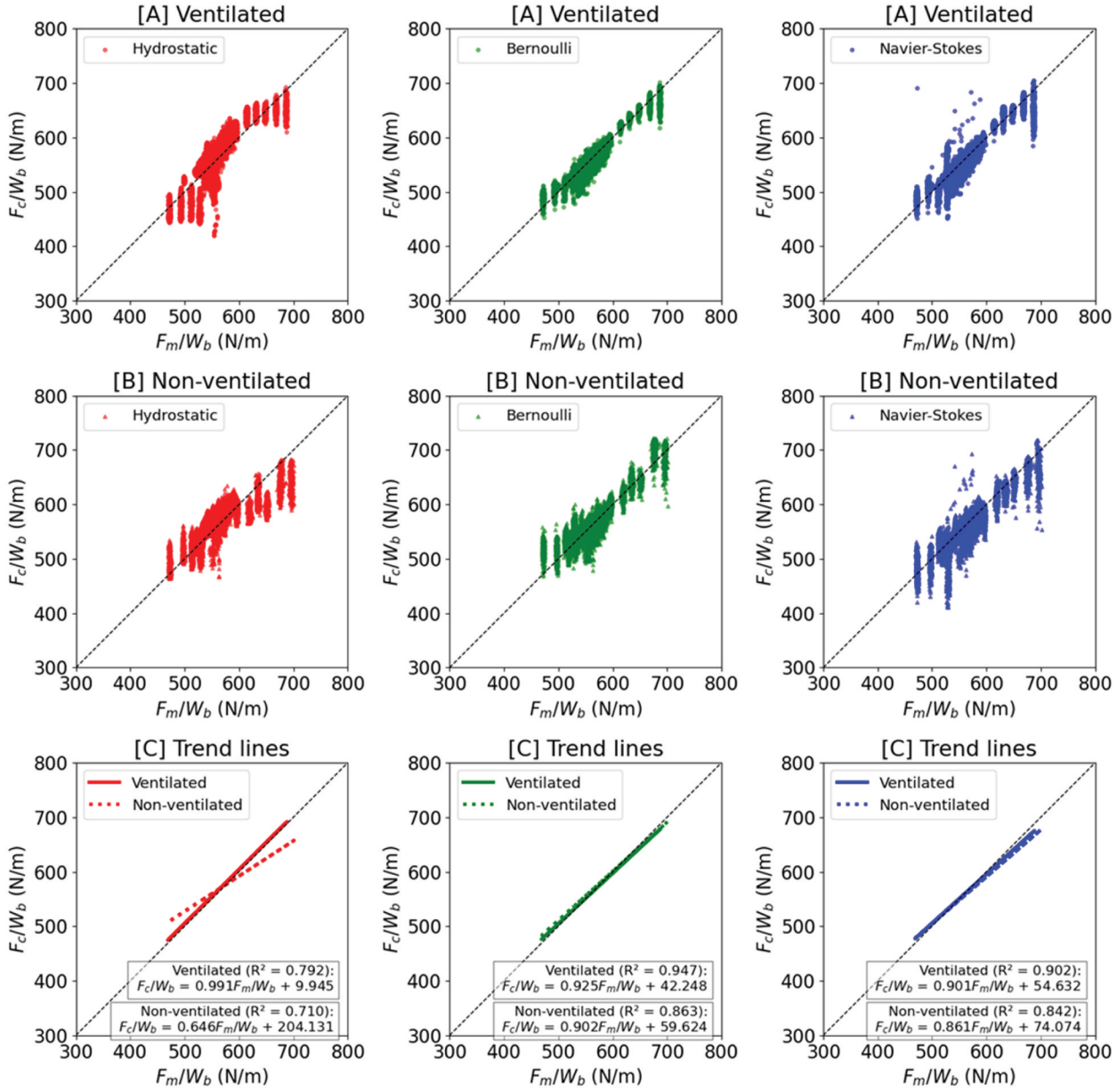

Figure 11. Linear regression analysis of measured force vs. calculated forces under the (a) ventilated and the (b) Non-ventilated conditions, and (c) trend lines based on different pressure profiles (red: hydrostatic, Green: Bernoulli, blue: Navier-Stokes).

per unit width (F_m/W_b) and the y-axis denoting the calculated forces (F_c/W_b), while the results of the regression curve and the r-squared values are presented in Table 4.

In the ventilated case, the regression analysis from Table 4 reveals that the Hydrostatic pressure profile exhibits a slope of 0.991 and an intercept of 9.945 N/m, indicating a moderately strong relationship with an R-squared value of 0.792. Conversely, the Bernoulli equation-based pressure profile shows a higher R-squared value of 0.947, suggesting a better fit with its slope of 0.925 and intercept of 42.248 N/m. Similarly, the Navier–Stokes equation-based profile demonstrates a strong relationship with an R-squared value of 0.902, with a slope of 0.901 and an intercept of 54.632 N. The hydrostatic pressure profile emerges as the best fit, evidenced by its slope (0.991) and intercept values (9.945) being closest to 1 and 0, respectively. This suggests that the hydrostatic model provides the most accurate representation of the relationship between measured and calculated forces in ventilated conditions. The relatively lower regression slope of the Bernoulli and Navier–Stokes equations in this scenario can be attributed to the minimal impact of air-bubble movement on velocity within the recirculation pool in ventilated conditions. This indicates that the complexities added by the Bernoulli and Navier–Stokes models may not be necessary to capture the dynamics of the ventilated case effectively. In contrast, in the non-ventilated case, the hydrostatic pressure profile exhibits a slope of 0.646 and an intercept of 204.131 N/m, suggesting a poor fit, with a lower R-squared value of 0.710.

Table 4. Comparison of linear regression results for measured and calculated forces per unit width under different downstream pressure profile and ventilated conditions.

		Linear Regression equation			
Ventilation	Downstream pressure profile	Equation	Slope (a)	Intercept (b)	R-squared
Ventilated	Hydrostatic	$\frac{F_c}{W_b} = a\frac{F_m}{W_b} + b$	0.991	9.945	0.792
	Bernoulli	F_m: Measured force	0.925	42.248	0.947
	Navier-Stokes	F_c: Calculated force	0.901	54.632	0.902
Non-ventilated	Hydrostatic	W_b: Weir width	0.646	204.131	0.710
	Bernoulli		0.902	59.624	0.863
	Navier-Stokes		0.861	74.074	0.842

Conversely, the Bernoulli equation-based profile demonstrates a significantly higher R-squared value of 0.863, indicating a stronger relationship, with a slope of 0.902 and an intercept of 59.624 N. Similarly, the Navier–Stokes equation-based profile also shows a strong relationship, with an R-squared value of 0.842, a slope of 0.861, and an intercept of 74.074 N. In the Non-ventilated case, both the Bernoulli and Navier–Stokes equations exhibit the best results among the models, with their slope and intercept values aligning more closely with the expected values. This highlights the importance of utilizing methods that incorporate dynamics, such as the Bernoulli equation or Navier–Stokes equation in non-ventilated conditions, where air bubble movement within the recirculation pool significantly affects velocity. Employing the Hydrostatic pressure profile results in considerable errors between the actual values and the estimated ones.

6. Discussion

The central finding of this experiment highlight two main points. Firstly, under ventilated condition, the conventional practice of employing the hydrostatic pressure assumption to estimate the pressure profile on the downstream wall generally yields satisfactory results, aligning well with established practices. However, under non-ventilated conditions, the dynamic movement of air bubbles within the recirculation pool presents challenges. Here, using the hydrostatic pressure assumption often results in significant discrepancies when compared to measured values.

Before delving into the detailed discussion of the experimental results, it is important to explain why the variation in the calculated force, based on the pressure profile, is larger than the measured force. This discussion will cover three key factors that could influence the experimental outcomes: 1) an exploration of the conditions under which the results obtained in this study can be reliably applied is conducted. 2) the limitations of the data utilized in this research are addressed. 3) an examination is undertaken to understand why the accuracy of the Navier–Stokes equation, theoretically considered the most precise, falls short in certain instances.

6.1. Variation in calculated force

In Figure 11, while the variation in the measured force is small, the variation in the calculated force is large. To understand this, Figure 12 presents the time-series data for Group 2, comparing the calculated force and measured force, and decomposing the calculated force into its constituent terms based on Eqs. (7)–(8b). The top panels of Figure 12 show the time-series data for the total calculated force (solid lines) and the measured force (dashed lines). Since the calculated force is derived under hydrostatic conditions, the difference between the calculated and measured forces is more pronounced in the non-ventilated case compared to the ventilated case. Overall, the trends of the graphs are similar. However, as observed in Figure 11, the variation in the calculated force is larger than that in the measured force.

For the upstream water depth term Eq. (7), under ventilated conditions (A), it fluctuates around 600 to 640 N/m, showing significant variations over time. These fluctuations reflect the dynamic changes in the upstream water depth, directly impacting the total calculated force. The variation range of approximately 40 N/m indicates that even small changes in upstream water depth have a substantial effect on the calculated force. In non-ventilated conditions (B), the upstream water depth term ranges between 590 and 670 N/m, with more pronounced variations, reflecting the greater instability and larger fluctuations in upstream water depth. The variation range of about 80 N/m is larger than in the ventilated case, indicating a higher sensitivity to changes in upstream water depth.

The cavity water depth term Eq. (8a) in the ventilated condition fluctuates between −35 and −20 N/m, showing relatively small variations. This term has a stabilizing effect on the calculated force, but its contribution is negative, reducing the overall force. The relatively narrow range of about 15 N/m indicates less variability and a smaller impact on the total force variation compared to other terms. In non-ventilated conditions, the cavity water depth term varies between −45 and −25 N/m, with more significant fluctuations than in the ventilated condition. The larger range of about 20 N/m suggests that changes in cavity water depth have a more considerable impact on the

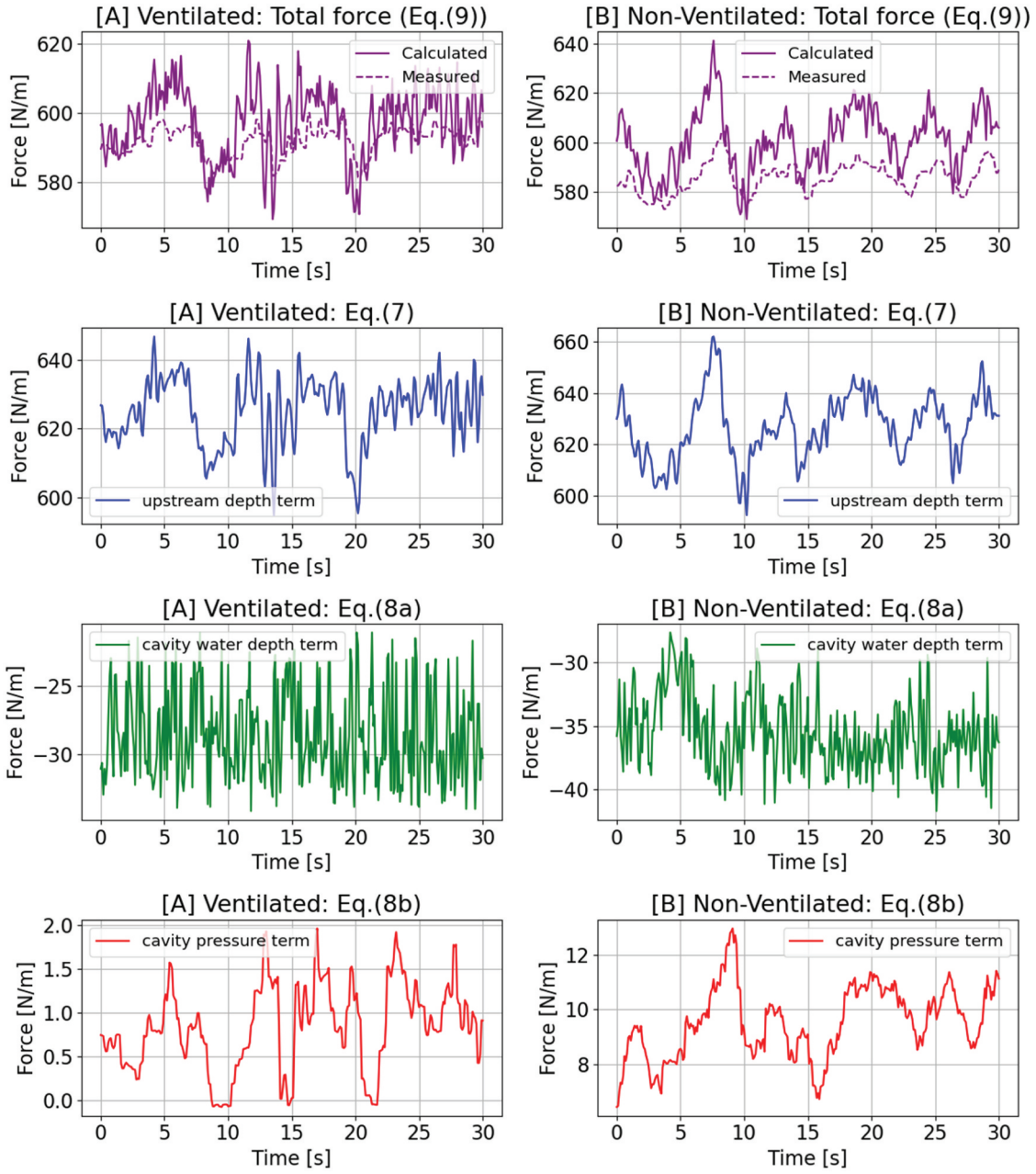

Figure 12. Time-series data of key factors influencing force calculations: (a) ventilated conditions, (b) non-ventilated conditions. Top panels show the total calculated force (solid) and measured force (dashed). The subsequent rows show the contributions of the upstream water depth term, cavity water depth term, and air cavity pressure term, respectively.

calculated force in non-ventilated conditions. This term still contributes negatively but with more variability, influencing the overall force stability.

The air cavity pressure term Eq. (8b) under ventilated conditions fluctuates around 0 to 2 N/m, indicating minimal impact. The small positive contributions and narrow variation range show that cavity pressure has a minor influence on the calculated force. In non-ventilated conditions, the air cavity pressure term ranges from 0 to 15 N/m, showing significant fluctuations. The larger range indicates a substantial impact on the calculated force, reflecting the dynamic changes in cavity pressure in non-ventilated conditions. This term adds positive contributions with high variability, affecting the overall force more significantly than in ventilated conditions.

Examining these time-series data reveals the dynamic interactions of these factors and their contributions to the overall variation in the calculated forces. The upstream water depth term exhibits the highest variability (~80 N/m), thus having the most substantial impact on the calculated force. The cavity water depth term, while stabilizing, introduces negative contributions with more variability (~20 N/m) in non-ventilated conditions. The air cavity pressure term has a minor influence under ventilated conditions but contributes significantly in non-ventilated conditions (~15 N/m). These insights clarify why the variation in calculated

forces is larger compared to measured forces, as the calculated forces are sensitive to instantaneous changes in these parameters. Additionally, it is important to note that the upstream water depth term dominates the total force calculation. The larger variance observed in the calculated forces is likely due to transverse variations in the upstream water level, which are not captured in the 2-D hydrostatic assumptions used for the calculations. In reality, the upstream water level can vary across the flume, leading to discrepancies between the calculated and measured forces. This transverse variation typically results in the total force being smaller than the calculated force, as 2-D assumptions tend to overestimate forces compared to more accurate 3-D calculations. These transverse variations in water level cause significant fluctuations in the calculated forces, further explaining the observed differences.

6.2. Verification of experimental conditions using dimensionless numbers and unit discharge

To successfully replicate the results of this study in other experiments, it is crucial to account for scale-dependent effects and ensure similarity between the current experiment and others. Here, the conditions under which this experiment was conducted are verified by providing dimensionless numbers at the brink of the weir.

Drawing from the methodology outlined by Mäkiharju et al. (2013), the Froude number, Weber number, and Reynolds number based on the brink of the broad-crested weir are defined in Eqs. (10a)–(10c) respectively. These equations consider definitions and the continuity equation, with all variables except for the upstream flow discharge (Q_{up}) and the water depth at the brink (h_{br}) treated as constants. These constants encompass gravity acceleration ($g = 9.81 {}^{m}/_{s^2}$), crest width ($W_b = 0.6m$), water density ($\rho = 1000 {}^{kg}/_{m^3}$), water surface tension ($\sigma = 72.8 {}^{mN}/_{m}$), and dynamic viscosity of water ($\mu = 1mPa \cdot s$).

$$Fr_{br} = \frac{U_{br}}{\sqrt{gh_{br}}} = \frac{Q_{up}}{\sqrt{g}(h_{br})^{1.5}W_b} = \frac{\sqrt{g}(h_c)^{1.5}W_b}{\sqrt{g}(h_{br})^{1.5}W_b} = \left(\frac{h_{crit}}{h_{br}}\right)^{1.5} \approx \left(\frac{h_{crit}}{0.715h_{crit}}\right)^{1.5} \tag{10a}$$

$$We_{br} = \frac{\rho(U_{br})^2 h_{br}}{\sigma} = \frac{\rho\left(Q_{up}\right)^2}{\sigma h_{br}(W_b)^2} \tag{10b}$$

$$Re_{br} = \frac{\rho U_{br} h_{br}}{\mu} = \frac{\rho Q_{up}}{\mu W_b} \tag{10c}$$

Here, the relationship between flowrate (Q_{up}) and critical depth (h_{crit}) is derived from the critical flow depth equation. The relationship between brink depth (h_{br}) and critical depth (h_{crit}) is based on Rouse's (1936) study ($h_{br} = 0.715h_{crit}$). Figure 13 presents the instantaneous values of dimensionless numbers derived from Equations (10a)–(10c) for both ventilated and non-ventilated conditions. The computed Froude, Weber, and Reynolds numbers indicate that the outcomes of this study will offer robust insights applicable to broad-crested weir scenarios, particularly when the Weber number at the brink falls within the range of 190 to 520. Surface tension is deemed negligible as the Weber number consistently exceeds the critical value of 120 (Jain, Garde, and Ranga Raju 1978). Therefore, the findings in this research are particularly relevant in scenarios where surface tension at the brink can be disregarded. The experiment yielded a Froude number at the brink depth of 1.654, indicating its suitability for broad-crested weir conditions. However, for sharp-crested weirs, where the theoretical Froude number at the brink depth is 1, the applicability of this study's results may be limited. Additionally, the Reynolds numbers obtained indicate fully turbulent flow conditions across all cases, with values exceeding 4000 at the brink. Therefore, the results are well-aligned with scenarios involving broad-crested weirs where the Froude number at the brink exceeds 1, the Weber number surpasses 120, allowing surface tension to be neglected, and the Reynolds number is greater than 4000, ensuring fully turbulent flow. Anderson and Tullis (2018) and Lodomez et al. (2019) have highlighted that in weir overflow scenarios, considering parameters like unit flow discharge instead of dimensionless numbers like Froude number might better account for scale effects. To address this, the unit flow discharge utilized in this study is presented in Table 5 with corresponding groups. The results of this study are deemed applicable within a flow discharge range of 0.013 to 0.063 [m^2/s].

6.3. Limited data for subcritical downstream case

Among the four groups used in this experiment, only one group, Group 4, employed the subcritical downstream regime, while the remaining three groups (Group 1 to 3) had supercritical downstream regimes. From the experimental results, it was observed that the flume outlet height, which is one of the independent variables, did not influence the forces acting on the broad crested weir in the supercritical downstream regime. However, in the subcritical downstream regime, the results revealed that the flume outlet height affects the weir forces by impacting the cavity water depth. However, due to the absence of experiments conducted specifically under subcritical downstream conditions by varying the outlet height, the exact relationship between the flume outlet height and its influence on the forces remains unconfirmed, posing an important issue to be addressed.

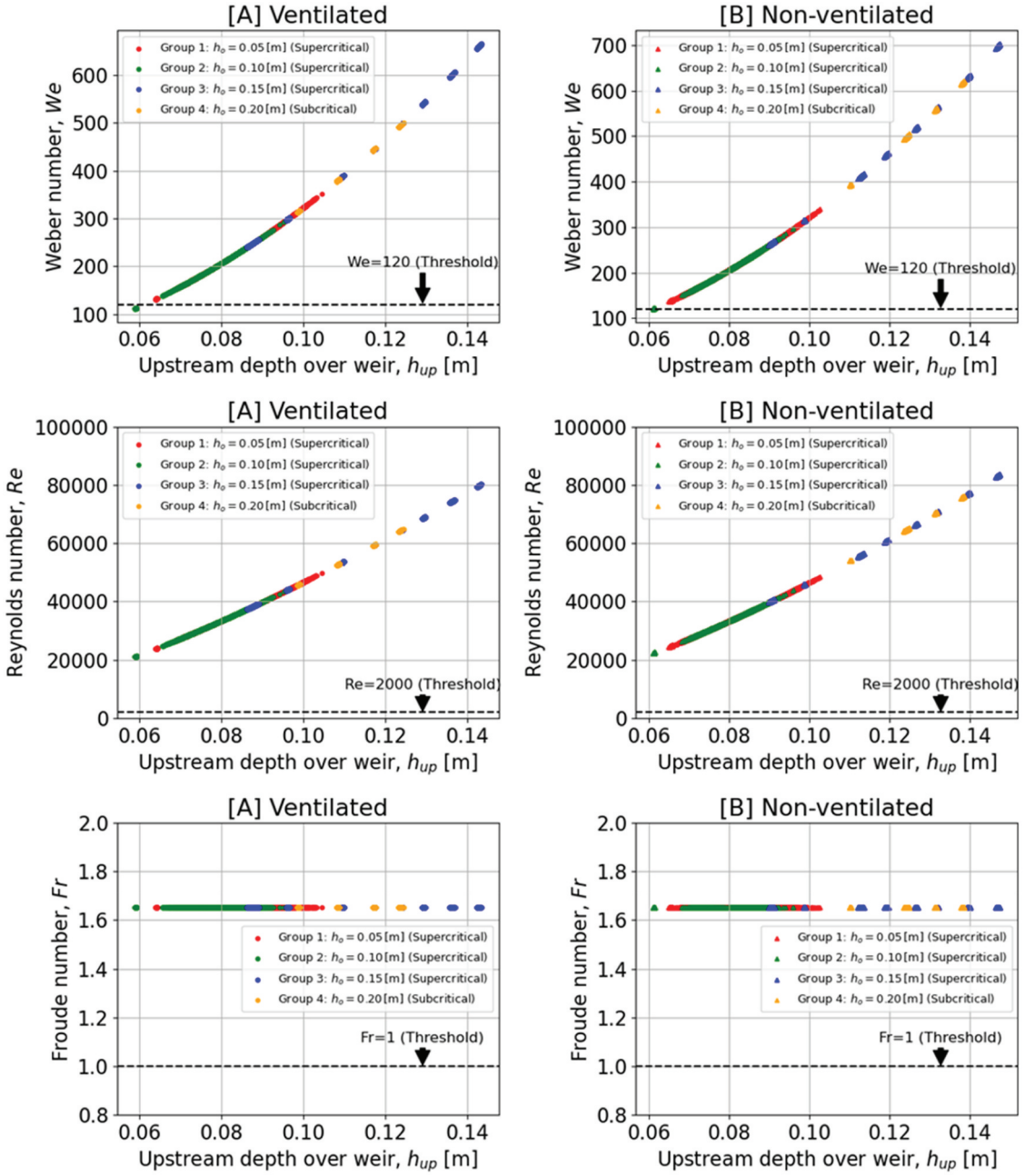

Figure 13. Instantaneous values of dimensionless numbers (Weber, Reynolds, Froude) under (a) ventilated and the (b) non-ventilated conditions.

Table 5. Unit flow discharge under the (A) ventilated and the (B) non-ventilated conditions.

Groups	Outlet height h_o [m]	Unit flow discharge [m^2/s]	
		[A] Ventilated	[B] Non-ventilated
Group 1	0.05	0.014 ~ 0.031	0.013 ~ 0.032
Group 2	0.10	0.013 ~ 0.027	0.014 ~ 0.025
Group 3	0.15	0.021 ~ 0.062	0.022 ~ 0.063
Group 4	0.20	0.022 ~ 0.043	0.022 ~ 0.045

6.4. Discrepancies

The results of this experiment revealed that for the Ventilated case, integrating the downstream pressure profile using the hydrostatic assumption yielded forces that exhibited the highest consistency with the measured values. In contrast, for the Non-ventilated case, employing the Bernoulli equation to compute the downstream pressure profile demonstrated the highest level of agreement with the measured forces. However, ideally, utilizing the Navier–Stokes equation to estimate the pressure profile and calculate the forces acting on the weir should yield the most optimal results for both

cases. This is because the Navier–Stokes equation is a more generalized equation that considers a broader range of factors. Two primary reasons for these differences are as follows: 1) cumulative errors from the use of multiple sensors, and 2) limitations of viscosity assumptions. Due to these factors, the performance of the Bernoulli equation was greater than that of the Navier–Stokes equation in this experiment.

6.4.1. Cumulative errors from the use of multiple sensors

In the ventilated cavity, the impact of air-bubble movement on the downstream wall of the weir is insignificant in this experiment. Here, dynamic terms such as flow velocity exert minimal influence on the pressure profile, with cavity water depth largely dominating. While the hydrostatic assumption relies solely on cavity water depth measurements for estimation, both the Bernoulli equation and Navier–Stokes equation utilize additional measurements, such as pressure sensors and the Bubble Image Velocimetry (BIV) method, to confirm observed pressure and velocity magnitude. Consequently, in scenarios like the Ventilated case where dynamic flow terms are relatively subdued, the accuracy of the Bernoulli equation or Navier–Stokes equation is not significantly higher than that of the hydrostatic assumption, mainly due to the cumulative errors associated with multiple sensors.

However, in the non-ventilated case, the vigorous movement of air bubbles elevates the importance of dynamic flow terms. Here, the accuracy of the Bernoulli equation or Navier–Stokes equation, which can account for dynamic terms, surpasses that of the hydrostatic assumption, even when considering cumulative sensor errors. This is because the hydrostatic assumption, relying solely on cavity water depth for pressure estimation, cannot adequately capture the influence of dynamic flow terms in scenarios characterized by active air bubble movement.

6.4.2. Limitations of eddy viscosity assumption

In the non-ventilated case, the slightly higher accuracy of the Bernoulli equation compared to the Navier–Stokes equation can be attributed to several factors. Theoretically, the Navier–Stokes equation, which accounts for eddy viscosity, should offer higher accuracy. The reason lies in the formula used to estimate eddy viscosity. Eddy viscosity is a property that is challenging to observe or estimate directly. In this experiment, to estimate eddy viscosity within the available experimental setup, a logarithmic layer assumption was made during the estimation of the mixing length, represented as $l_m = \kappa y$. While this assumption is suitable near the wall (less than 20% of the height of the flow), it becomes invalid in the outer layer (greater than 20% of the height of the flow). Furthermore, the water density was applied for the entire flow in the recirculation pool based on the conductivity probe results obtained from a single point. However, it is crucial to acknowledge that the momentum generated on the wall is influenced by the air-water mixture density. Data obtained from a single point may not adequately represent the entire flow, and consequently, assuming water density alone might lead to an overestimation of the momentum. Therefore, to enhance accuracy, additional measurements and alternative assumptions are required.

7. Conclusion

The comprehensive research conducted on the fluid dynamics of air-water flow during overflow of a broad-crested weir provides valuable insights for coastal and hydraulic engineer, particularly in the context of seawall, caisson breakwater, and weir design. By meticulously examining different flow regimes under both ventilated and non-ventilated conditions, this study illuminates the critical factors influencing the stability and integrity of such structures.

A key finding of this study is the significant role played by air–water interactions in the recirculation pool of a broad-crested weir. In ventilated conditions, the research demonstrated that forces exerted on the weir were predominantly dictated by upstream water depth, with outlet height having a minimal impact. This suggests that in designing weirs under similar conditions, emphasis should be placed on accurately measuring and modeling upstream water depths. The study also revealed that employing the hydrostatic pressure assumption to estimate the pressure profile on a ventilated weir's downstream wall yields results that are consistent with measured forces, underlining the practical utility of this traditional approach in ventilated scenarios.

In contrast, for non-ventilated conditions, the dynamics of air-water flow become significantly more complex. Here, the movement of air bubbles in the recirculation pool plays a vital role in influencing the pressure distribution and resultant forces on the weir. The study discovered that in these conditions, using the Bernoulli equation to compute the downstream pressure profile showed the highest level of agreement with measured forces. This highlights the need for more complex models that can account for dynamic flow parameters, especially in scenarios where air bubble movement is pronounced.

Dimensional analysis using Froude, Weber, and Reynolds numbers established the conditions under which this study's findings could be applied to similar scenarios. The applicability of the results is particularly relevant in broad-crested weir conditions with a Froude number at the brink exceeding 1, a Weber number surpassing 120 (negligible surface tension), and a Reynolds number greater than 4000 (fully turbulent).

In summary, this study provides crucial advancements in understanding the intricate dynamics of air-water flow in weir overflow scenarios, offering a foundation for improving the design and analysis of hydraulic structures. The insights gained from ventilated and non-ventilated conditions guide the choice of modeling approaches, emphasizing the need for accurate, dynamic modeling in complex flow environments. Further research, particularly in subcritical flow regimes and enhanced measurement techniques, will continue to refine and advance our understanding of these vital engineering challenges.

Acknowledgments

The authors extend their heartfelt gratitude to the laboratory technicians in the Civil and Environmental Engineering Department at the University of Michigan for their invaluable contributions. Special thanks go to Jan Pantolin for providing guidance on the use of experimental equipment. Additionally, Steve Donajkowski and Justin Roelofs offered valuable assistance in the fabrication of the broad crested weir used in the experiments. Ethan Kennedy's support in establishing the data acquisition system was greatly appreciated.

Disclosure statement

No potential conflict of interest was reported by the author(s).

ORCID

Taeksang Kim http://orcid.org/0000-0001-9461-6911
Stefan Felder http://orcid.org/0000-0003-1079-6658
Jeremy Bricker http://orcid.org/0000-0002-7503-6652

References

American Society of Civil Engineers. 2021. *Minimum Design Loads and Associated Criteria for Buildings and Other Structures, ASCE/SEI 7-22 Chapter 6: Tsunami Loads and Effects*.

Anderson, A., and B. P. Tullis. 2018. "Finite Crest Length Weir Nappe Oscillation." *Journal of Hydraulic Engineering* 144 (6): 04018020. https://doi.org/10.1061/(ASCE)HY.1943-7900.0001461.

Arikawa, T., M. Sato, K. Shimosako, I. Hasegawa, G. S. Yeom, and T. Tomita. 2012. "Failure Mechanism of Kamaishi Breakwaters Due to the Great East Japan Earthquake Tsunami." *Coastal Engineering Proceedings* 1 (33): 16. https://doi.org/10.9753/icce.v33.structures.16.

Bricker, J. D., M. Francis, and A. Nakayama. 2012. "Scour Depths Near Coastal Structures Due to the 2011 Tohoku Tsunami." *Journal of Hydraulic Research* 50 (6): 637–641. https://doi.org/10.1080/00221686.2012.721015.

Bricker, J. D., H. Takagi, E. Mas, S. Kure, B. Adriano, C. Yi, and V. Roeber. 2014. "Spatial Variation of Damage Due to Storm Surge and Waves During Typhoon Haiyan in the Philippines." *土木学会論文集 B2 (海岸工学)* 70 (2): I__231–I__235.

Bricker, J. D., H. Takagi, and J. Mitsui. 2013. "Turbulence Model Effects on VOF Analysis of Breakwater Overtopping During the 2011 Great East Japan Tsunami." In *Proceedings of the 2013 IAHR World Congress*. Chengdu, China, 10153.

Canny, J. 1986. "A Computational Approach to Edge Detection." *IEEE Transactions on Pattern Analysis & Machine Intelligence* 6:679–698. https://doi.org/10.1109/TPAMI.1986.4767851.

Chanson, H. 1996. *Air Bubble Entrainment in Free-Surface Turbulent Shear Flows*. Amsterdam, The Netherlands: Elsevier.

Chock, G., I. Robertson, D. Kriebel, M. Francis, and I. Nistor. 2013. *Tohoku, Japan, Earthquake and Tsunami of 2011: Performance of Structures Under Tsunami Loads*. Reston, VA, USA: American Society of Civil Engineers. June.

Disanayaka Mudiyanselage, S. 2017. *Effect of Nappe Non-Aeration on Caisson Sliding Force During Tsunami Breakwater Overtopping*. Master's thesis, Delft University of Technology. TU Delft Repositories. http://resolver.tudelft.nl/uuid:728416ce-fa4e-4459-ac56-2059b2fc10c3.

Falvey, H. T. 1980. Air-Water Flow in Hydraulic Structures. NASA STI/Recon Technical Report N, 81, 26429.

Felder, S., and H. Chanson. 2015. "Phase-Detection Probe Measurements in High-Velocity Free-Surface Flows Including a Discussion of Key Sampling Parameters." *Experimental Thermal & Fluid Science* 61:66–78. https://doi.org/10.1016/j.expthermflusci.2014.10.009.

Felder, S., and H. Chanson. 2017. "Scale Effects in Microscopic Air-Water Flow Properties in High-Velocity Free-Surface Flows." *Experimental Thermal & Fluid Science* 83:19–36. https://doi.org/10.1016/j.expthermflusci.2016.12.009.

Felder, S., B. Hohermuth, and R. M. Boes. 2019. "High-Velocity Air-Water Flows Downstream of Sluice Gates Including Selection of Optimum Phase-Detection Probe." *International Journal of Multiphase Flow* 116:203–220. https://doi.org/10.1016/j.ijmultiphaseflow.2019.04.015.

Galbraith, R. M., and M. R. Head. 1975. "Eddy Viscosity and Mixing Length from Measured Boundary Layer Developments." *Aeronautical Quarterly* 26 (2): 133–154. https://doi.org/10.1017/S0001925900007277.

Goda, Y. 2010. *Random Seas and Design of Maritime Structures*. Vol. 33. Tokyo, Japan: World Scientific Publishing Company.

Hess, F., R. M. Boes, and F. M. Evers. 2023. "Forces on a Vertical Dam Due to Solitary Impulse Wave Run-Up and Overtopping." *Journal of Hydraulic Engineering* 149 (7): 04023020. https://doi.org/10.1061/JHEND8.HYENG-13200.

Jain, A. K., R. J. Garde, and K. G. Ranga Raju. 1978. "Vortex Formation at Vertical Pipe Intakes." *Journal of the Hydraulics Division* 104 (10): 1429–1445. https://doi.org/10.1061/JYCEAJ.0005087.

Jayaratne, R., A. Abimola, T. Mikami, S. Matsuba, M. Esteban, and T. Shibayama. 2014. "Predictive Model for Scour Depth of Coastal Structure Failures Due to Tsunamis." *Coastal Engineering Proceedings* 1 (34): 56–56. https://doi.org/10.9753/icce.v34.structures.56.

Kim, T., J. N. Malherbe, S. Shimpalee, and J. D. Bricker. 2024. "Sub-Nappe Air Cavity Pressure and Cavity Water Depth During Caisson Breakwater Overtopping by a Tsunami." *Journal of Marine Science and Engineering* 12 (7): 1135. https://doi.org/10.3390/jmse12071135.

Kim, T., J. Malherbe, S. Shimpalee, and J. Bricker. 2022. "SUB-NAPPE AIR CAVITY PRESSURE DURING OVERFLOW of a VERTICAL STRUCTURE." *Coastal Engineering Proceedings* 37 (37): 4–4. https://doi.org/10.9753/icce.v37.papers.4.

Koen, J., D. E. Bosman, and G. R. Basson. 2019. "Artificial Aeration of Stepped Spillways by Crest Piers and Flares for the Mitigation of Cavitation Damage." *Journal of the South African Institution of Civil Engineering* 61 (2): 28–38. https://doi.org/10.17159/2309-8775/2019/v61n2a3.

Laali, A. R., and J. M. Michel. 1984. "Air Entrainment in Ventilated Cavities: Case of the Fully Developed 'Half-Cavity'." *Journal of Fluids Engineering* 106 (3): 327–335. https://doi.org/10.1115/1.3243123.

Latorre, R. 1997. "Ship Hull Drag Reduction Using Bottom Air Injection." *Ocean Engineering* 24 (2): 161–175. https://doi.org/10.1016/0029-8018(96)00005-4.

Lodomez, M., B. P. Tullis, B. Dewals, P. Archambeau, M. Pirotton, and S. Erpicum. 2019. "Nappe Oscillations on Free-Overfall Structures: Size Scale Effects." *Journal of Hydraulic Engineering* 145 (6): 04019022. https://doi.org/10.1061/(ASCE)HY.1943-7900.0001615.

Mäkiharju, S. A., B. R. Elbing, A. Wiggins, S. Schinasi, J. M. Vanden-Broeck, M. Perlin, and S. L. Ceccio. 2013. "On the Scaling of Air Entrainment from a Ventilated Partial Cavity." *Journal of Fluid Mechanics* 732:47–76. https://doi.org/10.1017/jfm.2013.387.

Mäkiharju, S. A., H. Ganesh, and S. L. Ceccio. 2017. "The Dynamics of Partial Cavity Formation, Shedding and the Influence of Dissolved and Injected Non-Condensable Gas." *Journal of Fluid Mechanics* 829:420–458. https://doi.org/10.1017/jfm.2017.569.

Matveev, K. I., T. J. Burnett, and A. E. Ockfen. 2009. "Study of Air-Ventilated Cavity Under Model Hull on Water Surface." *Ocean Engineering* 36 (12–13): 930–940. https://doi.org/10.1016/j.oceaneng.2009.06.004.

Michel, J. M. 1984. "Some Features of Water Flows with Ventilated Cavities. ASME." *Journal of Fluids Engineering* 106 (3): 319–326. https://doi.org/10.1115/1.3243122.

Papillon, B., M. Sabourin, M. Couston, and C. Deschenes. 2002. "Methods for Air Admission in Hydroturbines." In *The XXIst IAHR Symposium on Hydraulic Machinery and Systems Conference*, 6–11. September. Lausanne, Switzerland.

Patil, A., S. D. Mudiyanselage, J. D. Bricker, W. Uijttewaal, and G. Keetels. 2018. "Effect of Overflow Nappe Non-Aeration on Tsunami Breakwater Failure." *Coastal Engineering Proceedings* 36 (36): 18–18. https://doi.org/10.9753/icce.v36.papers.18.

Prandtl, L. 1925. "Bericht über Untersuchungen zur ausgebildeten Turbulenz." *ZAMM - Journal of Applied Mathematics and Mechanics / Zeitschrift für Angewandte Mathematik und Mechanik* 5 (2): 136–139. 7. https://doi.org/10.1002/zamm.19250050212.

Rouse, H. 1936. "Discharge Characteristics of the Free Overfall: Use of Crest Section as a Control Provides Easy Means of Measuring Discharge." *Civil Engineering* 6 (4): 257–260.

Ryu, Y., K. A. Chang, and H. J. Lim. 2005. "Use of Bubble Image Velocimetry for Measurement of Plunging Wave Impinging on Structure and Associated Greenwater." *Measurement Science and Technology* 16 (10): 1945. https://doi.org/10.1088/0957-0233/16/10/009.

Seed, R. B., R. G. Bea, A. Athanasopoulos-Zekkos, G. P. Boutwell, J. D. Bray, C. Cheung, and J. Wartman. 2008. "New Orleans and Hurricane Katrina. II: The Central Region and the Lower Ninth Ward." *Journal of Geotechnical and Geoenvironmental Engineering* 134 (5): 718–739. https://doi.org/10.1061/(ASCE)1090-0241(2008)134:5(718).

Stamhuis, E., and W. Thielicke. 2014. "PIVlab–Towards User-Friendly, Affordable and Accurate Digital Particle Image Velocimetry in MATLAB." *Journal of Open Research Software* 2 (1): 30. https://doi.org/10.5334/jors.bl.

Suppasri, A., S. Koshimura, K. Imai, E. Mas, H. Gokon, A. Muhari, and F. Imamura. 2012. "Damage Characteristic and Field Survey of the 2011 Great East Japan Tsunami in Miyagi Prefecture." *Coastal Engineering Journal* 54 (1): 1250005–1. https://doi.org/10.1142/S0578563412500052.

Takagi, H. 2015. "Method for Quick Assessment of Caisson Breakwater Failure Due to Tsunamis: Retrospective Analysis of Data from the 2011 Great East Japan Earthquake and Tsunami." *Coastal Engineering Journal* 57 (3): 1550012–1. https://doi.org/10.1142/S0578563415500126.

Tanimoto, K., and S. Takahashi. 1994. "Design and Construction of Caisson Breakwaters—The Japanese Experience." *Coastal Engineering* 22 (1–2): 57–77. https://doi.org/10.1016/0378-3839(94)90048-5.

Thielicke, W. 2014. *The Flapping Flight of Birds - Analysis and Application*. Phd thesis, Rijksuniversiteit Groningen. http://irs.ub.rug.nl/ppn/382783069.

Thielicke, W., and R. Sonntag. 2021. "Particle Image Velocimetry for MATLAB: Accuracy and Enhanced Algorithms in PIVlab." *Journal of Open Research Software* 9 (1): 12. https://doi.org/10.5334/jors.334.

Yoshida, K., S. Maeno, T. Iiboshi, and D. Araki. 2018. "Estimation of Hydrodynamic Forces Acting on Concrete Blocks of Toe Protection Works for Coastal Dikes by Tsunami Overflows." *Applied Ocean Research* 80:181–196. https://doi.org/10.1016/j.apor.2018.09.001.

Zou, P., T. Kim, J. D. Bricker, and W. S. Uijttewaal. 2023. "Assessment of Interfacial Turbulence Treatment Models for Free Surface Flows." *Journal of Hydraulic Research* 61 (5): 651–667. https://doi.org/10.1080/00221686.2023.2246925.